nature communications

Article

https://doi.org/10.1038/s41467-025-65451-2

Regenerating liver uses ammonia to support de novo pyrimidine synthesis and cell proliferation

Received: 4 August 2024

Accepted: 16 October 2025

Published online: 04 November 2025

Check for updates

Berwini B. Endaya[1,2,3,16] ✉, Lukáš Kučera[4,16], Dan-Diem Thi Le[1,2,16], Jessica B. Spinelli[5], Andrea Brožková[2], Dominika Luptáková[6], Kryštof Klíma[4], Gabriela L. Oliveira[1,7,8,9], Petra Brisudová[1], Klára Boháčová[1], Štěpána Boukalová[1], Renata Zobalová[1], František Kolář[10], Karel Chalupsky[4], Klára Dohnalová[4], Arash Yarmohammadi-Barzegar[2], Šárka Dvořáková[1], Evgeniya Biryukova[4], Marta Kaliaeva[4], Vladimír Havlíček[6,11], Radislav Sedláček[4], Jan Procházka[4], Libor Vítek[3,12], Sunghyouk Park[13], Pavel Martásek[3,12], Zdeněk Krška[3,12], Paulo J. Oliveira[7,8], Michael V. Berridge[14] & Jiří Neužil[1,2,3,15] ✉

Liver is endowed with high regenerative activity, so that the tissue regrows in mouse after partial hepatectomy within days. We reason that this requires de novo pyrimidine synthesis to support rapid progression via the cell cycle. We find that suppression of de novo pyrimidine synthesis prevents proliferation in regenerating liver, suppressing liver regrowth. Tracing studies and spatial metabolomics reveal a metabolic shift such that ammonia, normally detoxified to urea in the periportal region under homeostasis, is redirected for generating aspartate and carbamoyl phosphate periportally, and glutamine pericentrally, and these products are utilized as precursors by the de novo pyrimidine synthesis pathway. Our research uncovers a metabolic reprogramming leading to utilization of a toxic byproduct for anabolic pathways that are essential for liver regeneration.

The liver exhibits a remarkable capacity for complete regeneration following partial hepatectomy (PHx). In murine models, routinely used for investigating liver regeneration[1], restoration of the tissue after ~ 35% PHx is achieved within a timeframe of fewer than seven days. This rapid proliferation surpasses even the robust growth observed in fast-proliferating tissues such as tumors. However, unlike tumors, the liver ceases to grow upon reaching its original mass, determined by cell number[2–4]. Liver regeneration involves in its initial phase a stage referred to as compensatory cellular hypertrophy (CCH), which results in rapid liver expansion after PHx due to increased hepatocyte size,

[1]Institute of Biotechnology, Czech Academy of Sciences, Prague-West, Czech Republic. [2]Faculty of Science, Charles University, Prague, Czech Republic. [3]First Faculty of Medicine, Charles University, Prague, Czech Republic. [4]Institute of Molecular Genetics, Academy of Sciences of the Czech Republic, Prague, Czech Republic. [5]Worcester Chan Medical School, University of Massachusetts, Cambridge, MA, USA. [6]Institute of Microbiology, Czech Academy of Sciences, Prague, Czech Republic. [7]CNC-UC, Center for Neuroscience and Cell Biology, University of Coimbra, Coimbra, Portugal. [8]CIBB, Center for Innovative Biomedicine and Biotechnology, University of Coimbra, Coimbra, Portugal. [9]PDBEB - Doctoral Programme in Experimental Biology and Biomedicine, Institute of Interdisciplinary Research, University of Coimbra, Coimbra, Portugal. [10]Institute of Physiology, Czech Academy of Sciences, Prague, Czech Republic. [11]Faculty of Science, Palacký University, Olomouc, Czech Republic. [12]General University Hospital, Prague, Czech Republic. [13]College of Pharmacy, Natural Product Research Institute, Seoul National University, Seoul, Korea. [14]Malaghan Institute of Medical Research, Kelburn, Wellington, New Zealand. [15]School of Pharmacy and Medical Science, Griffith University, Southport, Qld, Australia. [16]These authors contributed equally: Berwini B. Endaya, Lukáš Kučera, Dan-Diem Thi Le. ✉e-mail: berwini.endaya@ibt.cas.cz; jiri.neuzil@ibt.cas.cz

followed by the phase of robust proliferation[5–7]. Not surprisingly, regeneration of liver tissue after PHx involves altered metabolism to support this highly dynamic process by engaging in particular anabolic pathways[8–11]. Both cell growth to a larger size and proliferation are dependent on mitochondrial function[12,13].

The de novo pyrimidine synthesis pathway is important for cell proliferation to provide nucleic acid precursors. Not much is known about its role in liver regeneration. We have recently found that cancer cells with dysfunctional mitochondria import these organelles with their DNA payload via horizontal mitochondrial transport[14,15], in order to restore mitochondrial respiration that is critically linked to de novo pyrimidine synthesis, enabling transition through the S-phase of the cell cycle[15]. It can be estimated that approximately half a billion cells need to form in the mouse liver within the span of < 7 days following ~35% PHx. Consequently, we postulated that such robust cell growth necessitates the engagement of de novo pyrimidine synthesis for rapid transition through the cell cycle.

We show here the critical role of de novo pyrimidine synthesis in liver regeneration linked to rapid metabolic remodeling, whereby detoxification of ammonia in the liver is suppressed in favor of the use of this toxic product to support anabolic pathways epitomized by the de novo pyrimidine pathway.

Results

Inhibition of dihydroorotate dehydrogenase suppresses liver regeneration

Our recent research showed that de novo pyrimidine synthesis (see scheme in Fig. 1a) is of importance for tumor formation that cancer cells devoid of mitochondrial DNA (mtDNA) import mitochondria with DNA from the surrounding stroma to restore respiration needed to drive conversion of dihydroorotate (DHO) to orotate. This is catalyzed by dihydroorotate dehydrogenase (DHODH), an enzyme coupled to the mitochondrial electron redox chain[16]. Since it takes 5–7 days to fully regenerate liver after removal of the left lateral lobe (Fig. 1b), which equates to about ~35% PHx[17], we anticipated that generation of the high number of cells requires a switch from homeostasis to metabolic pathways that support rapid cell proliferation required for fast transition via the cell cycle, supported by de novo pyrimidine synthesis. It has been shown that inhibition of DHODH, using the specific inhibitor BAY-2402234 that suppresses activity of the enzyme with an IC_{50} of 3–5 nM[18], results in suppression of tumor growth[19]. We therefore tested the effect of the inhibitor on liver regeneration following ~35% PHx (Fig. 1a, b). Figure 1c shows that the loss in body weight after PHx of about 1 g (assuming mouse weight of ~20 g) was followed by recovery to near that of control mice within 5 days. On the other hand, BAY-2402234 given to mice post-PHx by daily gavage (2 or 5 mg/kg) resulted in a complete halt in body weight increase. This is further corroborated by the liver to body weight ratio (LBWR), where the full restoration of liver in mice at 7 days is blocked by the DHODH inhibitor (Fig. 1d). Of note, treated mice exhibited similar liver status parameters compared to untreated mice 3–14 days after ~35% PHx (Supplementary Fig. 1) and had a 100% survival rate (Supplementary Fig. 2), suggesting that treatment with BAY-2402234 following 35% PHx is well tolerated and does not cause toxicity[18].

To test whether the DHODH inhibitor specifically blocks cell proliferation in liver tissue following PHx, we probed for known proliferation markers such as minichromosome maintenance complex component 2 (MCM2), proliferating cell nuclear antigen (PCNA), and phospho-histone H3 (pHH3), and performed an EdU (5-ethynyl-2′-deoxyuridine) assay[20]. The results demonstrate robust proliferation in regenerating liver peaking on day 3 after PHx, with slower proliferation on day 7 (Fig. 1e, f), and tissue distribution of proliferation encompassing whole liver parenchyma from periportal to pericentral localizations (Fig. 1g and Supplementary Fig. 3a). Treatment with BAY-2402234 considerably suppressed proliferation, as shown in Fig. 1e, f and Supplementary Fig. 3b.

De novo pyrimidine pathway is required for liver regeneration

We next investigated whether BAY-2402234 suppresses de novo pyrimidine synthesis (see scheme in Fig. 1a) in the context of liver regeneration. We first assessed the effect of the inhibitor on DHODH-dependent respiration (Fig. 2a) and DHODH activity (Fig. 2b), and found that suppression of both parameters considerably lowered the orotate-to-DHO ratio (Fig. 2c).

To extend our studies further, we applied LC-MS and MALDI imaging techniques to determine levels of de novo pyrimidine pathway intermediates. Figure 2d shows the level of glutamine (Gln), carbamoyl aspartate (CA), DHO and uridine monophosphate (UMP) in control liver and in liver on days 3, 7 and 14 post-PHx, as well as on day 3 after PHx in mice treated with BAY-2402234. LC-MS data show progressive increase in liver levels of Gln, CA and DHO from day 3 to day 7 post-PHx, followed by a reduction in levels similar to control on day 14 post-PHx. Interestingly, MALDI imaging analyses show high levels of aspartate (Asp), carbamoyl phosphate (CP), CA and DHO (also shown by LC-MS), precursors of orotate formed from DHO by DHODH, coupled with low levels of UMP and uridine diphosphate (UDP) on day 3 PHx mice treated with the DHODH inhibitor (Fig. 2d and Supplementary Fig. 4). Spatial mapping by combined MALDI imaging and immunostaining localized Gln pericentrally and glutamate (Glu) periportally in control and day 3 post-PHx with and without BAY-2402234 treatment (Fig. 2e). Notably, the high levels of orotate precursors observed in BAY-2402234-treated liver 3 days post-PHx exhibited differential localization. While CA and DHO were distributed across the whole liver parenchyma, aspartate (Asp) was mainly periportal, with its distribution similar in extent to Glu (Fig. 2e). We conclude from data in Figs. 1, 2, and Supplementary Fig. 4 that de novo pyrimidine synthesis is required for the proliferation of liver cells, and therefore for liver regeneration. In addition, as Asp and Glu are linked to the urea cycle, Asp accumulation periportally closely mirrors Glu spatial distribution upon BAY-2402234 treatment 3 days post-PHx, suggesting possible involvement of the urea cycle in fulfilling this requirement for de novo pyrimidine synthesis.

Urea cycle activity is lower in regenerating liver

A major liver function is detoxification of ammonia to urea. Since loss of hepatic tissue, e.g., due to resection, theoretically reduces its capacity to process ammonia, we queried the possibility of metabolic remodeling. Here, we hypothesize that the toxic metabolite ammonia, rather than being 'wasted' in the form of urea formed via the urea cycle (Fig. 3a), is utilized to support the increased demand for metabolic precursors necessary for anabolic pathway(s) of rapidly regenerating liver. To investigate this, we determined the state of the urea cycle during liver regeneration by treating mice with $^{15}NH_4Cl$, given by intraperitoneal injection, and analyzing liver tissue by LC-MS to assess the fate of unlabeled and labeled ammonium chloride in the context of the urea cycle. Interestingly, urea cycle activity, assessed as the ratio of citrulline and CA (Fig. 3b), and as a function of ornithine transcarbamoylase (OTC) activity (ratio of citrulline and ornithine) (Fig. 3c), is lower following PHx from day 3–7, with a tendency to normalize to control mouse liver levels on day 14 post-PHx. Importantly, this effect on the urea cycle activity is mirrored by the levels of urea in the circulation (Fig. 3d and Supplementary Fig. 5).

Lower urea cycle activity, and as a consequence, lower blood urea levels, is further corroborated by LC-MS data showing lower citrulline and arginosuccinate concurrent with increased ornithine levels on days 3 and 7 post-PHx, and restoration to control levels at day 14 post-PHx (Fig. 3e), thereby confirming lower activity of the urea cycle in ammonia detoxification on days 3 and 7 post-PHx, and normalization at the time of completed liver regeneration. Of note, similar metabolic tendencies were observed for m + 1 isotopologues of metabolites

https://doi.org/10.1038/s41467-025-65451-2

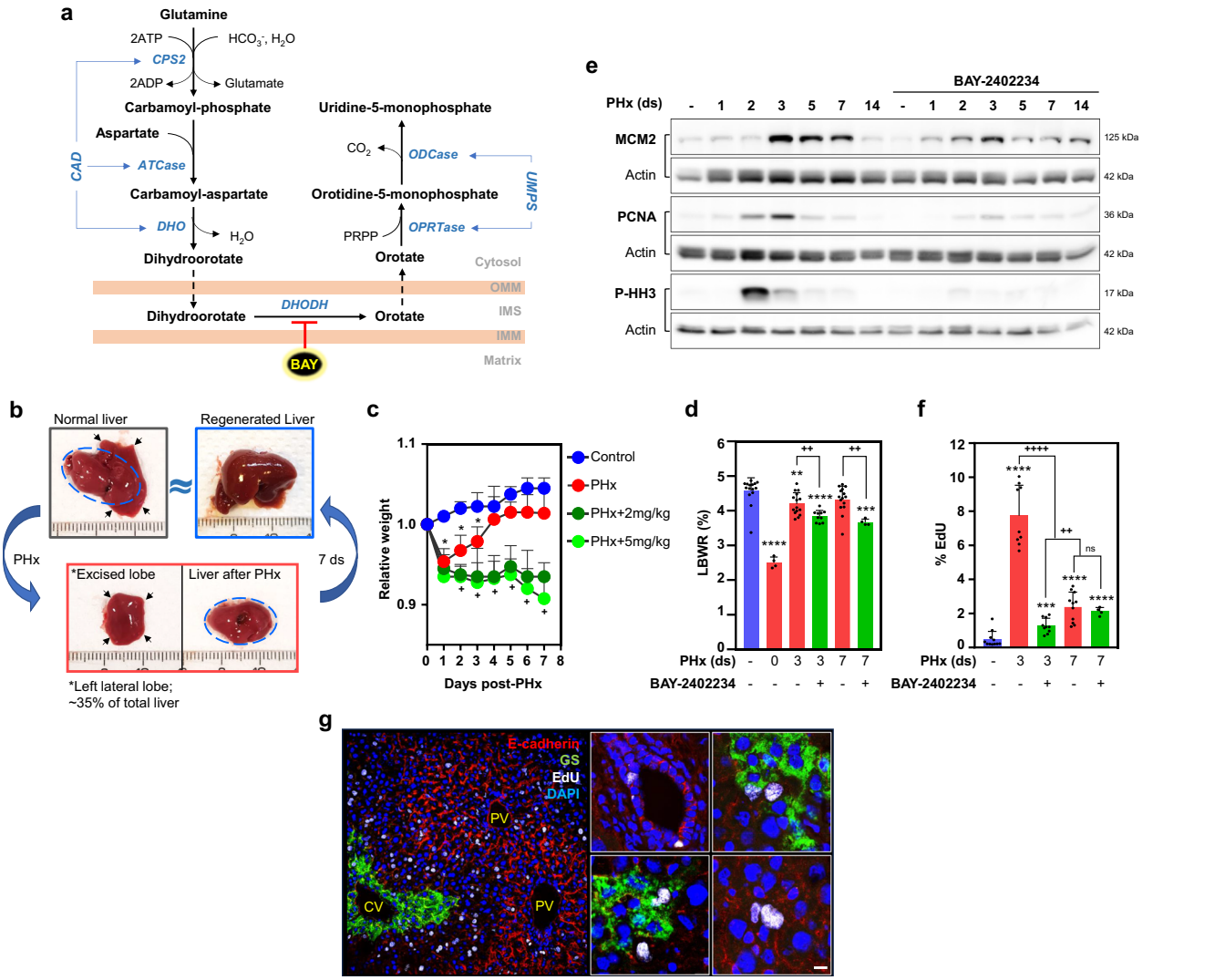

Fig. 1 | Liver regeneration and hepatocyte proliferation are suppressed by a DHODH inhibitor. a Scheme of the de novo pyrimidine pathway illustrating the precursor substrates and respective enzymes to make the final product uridine-5-monophosphate (UMP), which can be inhibited by BAY-2402234 (BAY) specifically targeting DHODH in the mitochondria. **b** Mouse liver subjected to partial hepatectomy (PHx) showing removal of the left lateral lobe (~35% of the whole liver) with full regeneration of the remaining liver occurring within 7 days. Relative body weight (**c**) and liver/bodyweight ratio (LBWR, %) (**d**) of control mice and mice subjected to ~ 35% PHx with or without daily gavage of BAY. Assessment of proliferation using western blot (WB) of MCM2, PCNA, and pHH3 (**e**), and using the EdU assay (**f**) in control and ~35% PHx mice with or without daily gavage of BAY at the indicated timepoints. **g** A section of regenerating liver was imaged for E-cadherin (red) to demarcate the periportal region surrounding the portal vein (PV), GS (green) to stain the pericentral cells surrounding the central vein (CV), and EdU-positive cells (white) showing spatial localization of proliferating cells encompassing periportal to pericentral distribution within the liver (inset). For panel (**c**), multiple *t* tests using the Holm-Sidak method were used (control $n = 4$, PHx $n = 8$, PHx + 2 mg/kg BAY $n = 4$, PHx + 5 mg/kg BAY $n = 4$; *p*-values for control vs. PHx at days 1, 2, and 3 post-PHx are 0.0003, 0.0025, and 0.0122 respectively; *p*-values for PHx vs. PHx+2 mg/kg BAY at days 2, 3, 4, 5, 6 and 7 post-PHx are 0.0362, 0.0075, 0.0057, 0.0009, 0.0003, and 0.0061, respectively; *p*-values for PHx vs. PHx + 5 mg/kg BAY at days 2, 3, 4, 5, 6 and 7 post-PHx are 0.0370, 0.0370, 0.0085, 0.0264, 0.0040, and 0.0018, respectively). For panels (**d** and **f**), unpaired *t* test was used (**d**: control $n = 15$, day 0 post-PHx $n = 4$, day 3 post-PHx $n = 15$, day 3 post-PHx + 2 mg/kg BAY $n = 10$, day 7 post-PHx $n = 15$, day 7 post-PHx + 2 mg/kg BAY $n = 4$; *p*-values for control vs. post-PHx at days 0, 3, 3 + 2 mg/kg BAY, and 7 + 2 mg/kg BAY are < 0.0001, 0.0067, < 0.0001, and 0.0002, respectively; *p*-values for post-PHx day 3 vs. day 3 + 2 mg/kg BAY and post-PHx day 7 vs. day 7 + 2 mg/kg BAY are 0.0036 and 0.0035, respectively; (**f**) control $n = 11$, day 3 post-PHx $n = 9$, day 3 post-PHx + 2 mg/kg BAY $n = 10$, day 7 post-PHx $n = 11$, day 7 post-PHx + 2 mg/kg BAY $n = 4$; *p*-values for control vs. post-PHx days 3, 3 + 2 mg/kg BAY, 7, 7 + 2 mg/kg BAY are < 0.0001, 0.0007, < 0.0001, and < 0.0001, respectively; *p*-values for post-PHx day 3 vs. post-PHx day 3 + 2 mg/kg BAY, day 7, day 7 + 2 mg/kg BAY are < 0.0001; *p*-values for post-PHx day 3 + 2 mg/kg BAY vs. post-PHx day 7 and day 7 + 2 mg/kg BAY are 0.0017 and 0.0038, respectively). Images presented are representative of at least three independent biological experiments. Data are expressed as mean ± S.D. The symbols '*/+', '**/++', '***/+++', and '****/++++' denote statistical significance at $p < 0.05$, $p < 0.01$, $p < 0.001$, and $p < 0.0001$, respectively; ns, not significant. Source data are provided as a Source Data File.

(Fig. 3f), suggesting that the fate of injected ammonium chloride resembles metabolic processing of the unlabeled and presumably endogenous ammonia in the liver. Isotope fraction enrichment analysis confirms the metabolic processing of labeled ammonia via the urea cycle, and interestingly, demonstrated a more upstream enrichment of new intermediates made from the administered ammonia (Fig. 3g).

Ammonia that is not detoxified by urea cycle supports liver regeneration

The fact that the urea cycle activity is suppressed after PHx coupled with a tendency to a more upstream processing of new intermediates indicate that ammonia, which is detoxified via the urea cycle under homeostasis, can be redirected from upstream of the pathway towards

https://doi.org/10.1038/s41467-025-65451-2

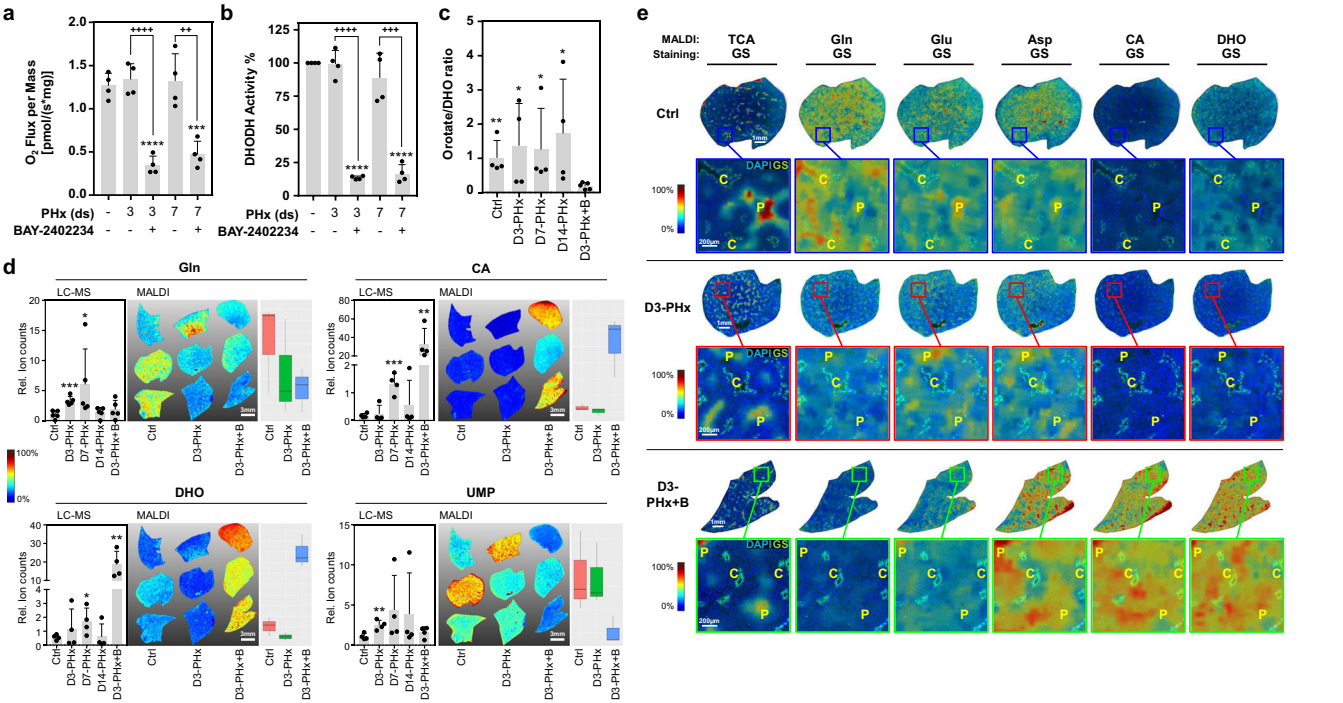

Fig. 2 | Liver regeneration requires de novo pyrimidine synthesis. Assessment of DHODH-dependent respiration (**a**), DHODH activity (**b**), and orotate-to-DHO ratio (**c**) in control mice and mice subjected to ~ 35% PHx with or without daily gavage of 2 mg/kg BAY-2402234 (BAY). LC-MS data showing levels of de novo pyrimidine metabolites glutamine (Gln), carbamoyl aspartate (CA), dihydroorotate (DHO), uridine monophosphate (UMP), their MALDI-TOF representative images with intensity quantification (**d**), and their MALDI-TOF spatial localization including glutamate (Glu) and aspartate (Asp) (**e**) demarcated by pericentral (C) GS staining (green), and periportal (P) taurocholic acid (TCA) accumulation in liver of control mice and mice subjected to ~ 35% PHx with or without daily gavage of 2 mg/kg BAY. MALDI-TOF images were acquired with the 9AA matrix and measured in the negative mode. Images are displayed with TIC normalization, 99% quantile hotspot removal, linear interpolation and weak denoising level. Peak intensities are rescaled to the full color map. For panels (**a**–**d**), unpaired *t* test was used, and data are expressed as mean ± S.D. (**a**: all groups have $n = 4$; control vs. day 3 post-PHx + 2 mg/kg BAY $p < 0.0001$; control vs. day 7 post-PHx + 2 mg/kg BAY $p = 0.0003$; day 3 post-PHx vs. day 3 post-PHx + 2 mg/kg BAY $p < 0.0001$; day 7 post-PHx vs. day 7 post-PHx + 2 mg/kg BAY $p = 0.0028$; **b**: all groups have $n = 4$; control vs. day 3 post-PHx + 2 mg/kg BAY $p < 0.0001$; control vs. day 7 post-PHx + 2 mg/kg BAY $p < 0.0001$; day 7 post-PHx vs. day 7 post-PHx + 2 mg/kg BAY $p = 0.0003$; **c**: control, post-PHx days 3, 7 and 14 have $n = 4$; day 3 post-PHx + 2 mg/kg BAY has $n = 5$; day 3 post-PHx + 2 mg/kg BAY vs. control $p = 0.0042$; day 3 post-PHx + 2 mg/kg BAY vs. day 3 post-PHx $p = 0.0034$; day 3 post-PHx + 2 mg/kg BAY vs. day 7 post-PHx $p = 0.0418$; day 3 post-PHx + 2 mg/kg BAY vs. day 14 post-PHx $p = 0.0319$; **d**, Gln: $n = 5$ for all groups; control vs. day 3 post-PHx $p = 0.0004$; control vs. day 7 post-PHx $p = 0.0476$; **d**, CA: $n = 4$ for all groups; control vs. day 7 post-PHx $p = 0.0004$; control vs. day 3 post-PHx + 2 mg/kg BAY $p = 0.0044$; **d**, DHO: $n = 4$ for all groups; control vs. day 7 post-PHx $p = 0.013$; control vs. day 3 post-PHx + 2 mg/kg BAY $p = 0.0011$; **d**, UMP: $n = 4$ for all groups; control vs. day 3 post-PHx $p = 0.0035$; boxplot in d: midline depicts median value; the lower and upper hinges correspond to the first and third quartiles, representing the 25th and 75th percentiles respectively; the upper whisker extends from the hinge to the largest value no further than 1.5 * IQR from the hinge; the lower whisker extends from the hinge to the smallest value at most 1.5 * IQR of the hinge). The symbols '*/+', '**/++', '***/+++', and '****/++++' denote statistical significance at $p < 0.05$, $p < 0.01$, $p < 0.001$, and $p < 0.0001$, respectively. Source data are provided as a Source Data File.

anabolic reactions to support liver regeneration. This intriguing scenario, where a toxic metabolite is repurposed 'in time of need' to generate additional substrate to support efficient generation of pyrimidines by the de novo pathway, was further investigated. Figure 4a shows schematically the metabolite fluxes involving the urea cycle and de novo pyrimidine synthesis, highlighting diversion of the ammonia flow into de novo pyrimidine synthesis during liver regeneration. In this scheme, the entry points of ammonia into the pathway are (i) direct amination of Glu to Gln, catalyzed by glutamine synthetase (GS); (ii) reductive amination of α-ketoglutarate (α-KG) to Glu catalyzed by glutamate dehydrogenase (GDH), which can further incorporate ammonia by its amination to Gln, or be incorporated into the pathway as Asp via transamination catalyzed by glutamic-oxaloacetic transaminase 1 (GOT1); and (iii) incorporation into CP catalyzed by carbamoyl phosphate synthetase 1 (CPS1) that, along with Asp, can give rise to CA via the second reaction of the trifunctional enzyme CAD. Expression of these enzymes, including those of the de novo pathway is similar in regenerating liver 3 to 14 days post-PHx including liver treated with BAY-2402234 for 3 days post-PHx compared to control (Supplementary Fig. 6), suggesting that their levels are maintained post-PHx even after treatment with BAY-2402234 at the indicated timepoints.

In accordance with the scheme, we evaluated the regenerating liver from $^{15}NH_4Cl$-injected mice for the presence of metabolites described, including their m + 1 and m + 2 isotopologues to track the flow of ammonia. Figure 4b shows the overall trend, whereby metabolites of de novo pyrimidine synthesis, Gln, DHO, orotate and UMP increase on days 3 and 7 post-PHx before normalizing to control levels on day 14, highlighting the need for de novo pyrimidines as the liver regenerates. A similar trend was observed for Asp, Glu and CA, suggesting the incorporation of ammonia into regenerating liver pyrimidine precursors via GDH and GOT1, and CPS1 in the urea pathway. Furthermore, the metabolic tendencies for the m + 1 and m + 2 isotopologues were similar to the unlabeled metabolites, pointing to direct incorporation of ammonia into the precursors shown in Fig. 4a. In addition, the accumulation of high levels of unlabeled and m + 1 and m + 2 DHO and CA coupled with low levels of UMP upon treatment with BAY-2402234 on day 3 provides further evidence for incorporation of ammonia into the de novo pyrimidine pathway. Analysis of the isotope fraction enrichment reveals that as much as ~50% of the new de

https://doi.org/10.1038/s41467-025-65451-2

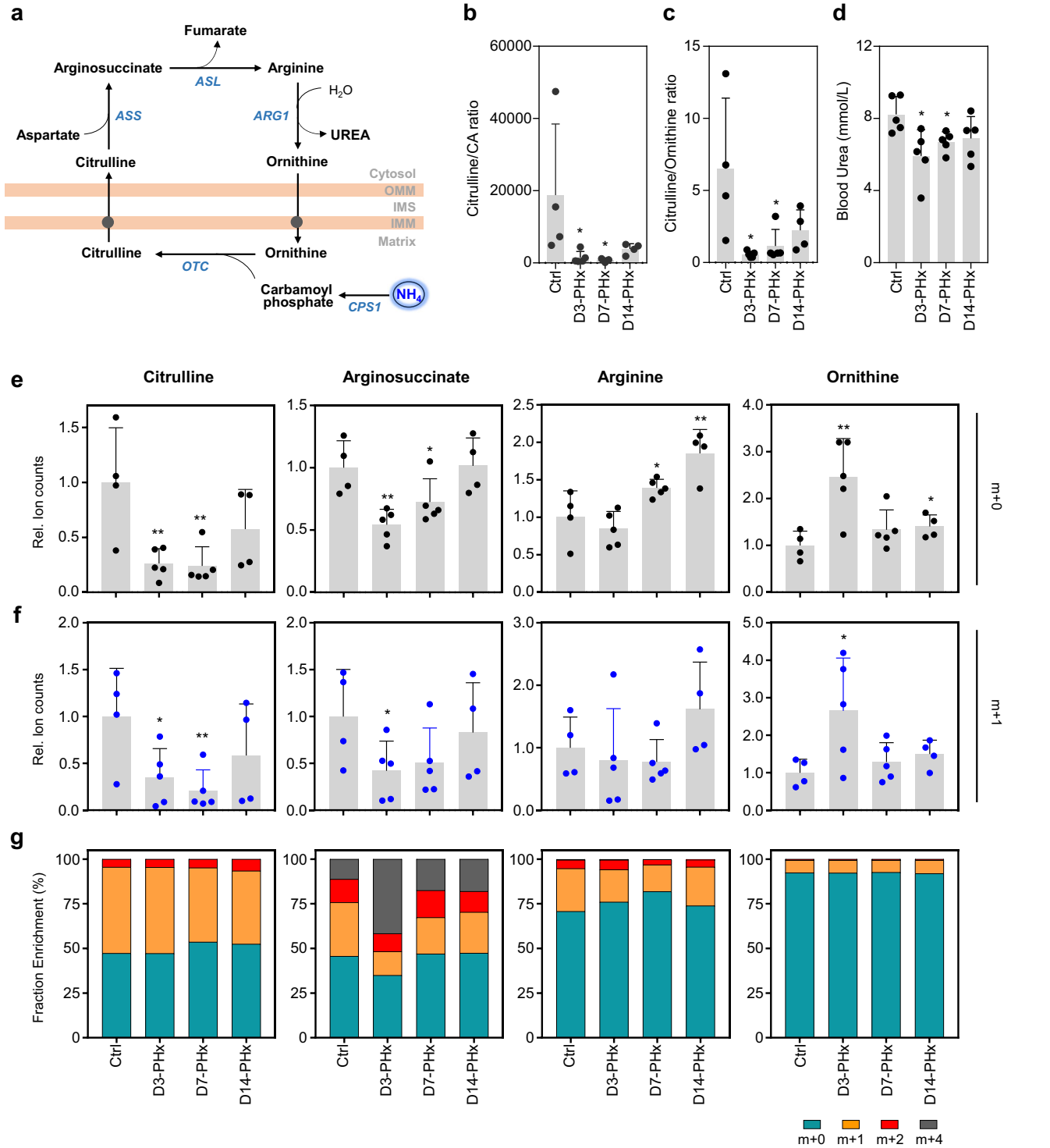

novo pyrimidine intermediates Gln, CA, DHO and orotate stemmed from the administered ammonia (Fig. 4c). These results show that during liver regeneration, ammonia is diverted from urea cycle detoxification towards anabolic processes to form pyrimidines via the de novo pathway, thus allowing for fast cell proliferation to facilitate liver regeneration following PHx.

Liver regeneration involves zoning of metabolic pathways

On the premise that liver function is zonal[21], where the urea cycle, dependent on CPS1 to 'scavenge' ammonia, is largely confined periportally, and Gln synthesis by GS strictly pericentrally, we propose that the entry points for ammonia incorporation to support de novo pyrimidine synthesis, and thus cell proliferation within regenerating liver, will be zonal as well (Fig. 5a; *cf*. Figure 1g and Supplementary Fig. 3a). This is further supported by our initial findings where Glu, an upstream urea cycle metabolite, localized periportally and Gln pericentrally (*cf*. Figure 2e). We mapped liver zones spanning periportal to pericentral localizations using specific functional markers glutaminase-2 (GLS2), GS, and CPS1 (Fig. 5b). While GLS2 and CPS1 co-localize periportally (Fig. 5b), CPS1 expression extends well beyond the GLS2 + periportal regions further into the parenchyma but is mutually exclusive with pericentral GS (Fig. 5c). This suggests that CPS1-mediated ammonia scavenging encompasses the majority of the hepatic zones, bounded only by the GS+ zone where it is not

Fig. 3 | Hepatectomy is followed by low activity of the urea cycle. a Scheme of the urea cycle showing the classical 'entry' of ammonia into the pathway as carbamoyl phosphate (CP), catalyzed by CPS1 and its eventual conversion into urea. Assessment of the urea cycle activity presented as a ratio of citrulline and carbamoyl aspartate (CA) (**b**), and as a ratio of citrulline and ornithine (OTC activity) (**c**), and the corresponding urea levels in the blood (**d**), analyzed in the liver or blood of control mice and mice subjected to ~ 35% PHx. **e**, **f** Evaluation of the m + 0 and m + 1 metabolites of the urea cycle following injection of $^{15}NH_4Cl$ in control mice and mice subjected to ~ 35% PHx. **g** Isotope ratio reported as fraction enrichment (%) of all possible nitrogen isotope variations. For panels (**b**–**f**), unpaired *t* test was used and data are expressed as mean ± S.D. (**b**: control, day 14 post-PHx $n = 4$; day 3 post-PHx, day 7 post-PHx $n = 5$; control vs. day 3 post-PHx $p = 0.0431$; control vs. day 7 post-PHx $p = 0.0374$; **c**: control, day 14 post-PHx $n = 4$; day 3 post-PHx, day 7 post-PHx $n = 5$; control vs. day 3 post-PHx $p = 0.0140$; control vs. day 7 post-PHx $p = 0.0234$; **d**: all groups have $n = 5$; control vs. day 3 post-PHx $p = 0.0191$; control vs. day 7 post-PHx $p = 0.0173$; **e**, Citrulline: control, day 14 post-PHx $n = 4$; day 3 post-PHx, day 7 post-PHx $n = 5$; control vs. day 3 post-PHx $p = 0.0072$; control vs. day 7 post-PHx $p = 0.0072$; **e**, Arginosuccinate: control, day 14 post-PHx $n = 4$; day 3 post-PHx, day 7 post-PHx $n = 5$; control vs. day 3 post-PHx $p = 0.0025$; control vs. day 7 post-PHx $p = 0.0397$; **e**, Arginine: control, day 14 post-PHx $n = 4$; day 3 post-PHx, day 7 post-PHx $n = 5$; control vs. day 7 post-PHx $p = 0.0250$; control vs. day 14 post-PHx $p = 0.0057$; **e**, Ornithine: control, day 14 post-PHx $n = 4$; day 3 post-PHx, day 7 post-PHx $n = 5$; control vs. day 3 post-PHx $p = 0.0060$; control vs. day 14 post-PHx $p = 0.0425$; **f**, Citrulline: control, day 14 post-PHx $n = 4$; day 3 post-PHx, day 7 post-PHx $n = 5$; control vs. day 3 post-PHx $p = 0.0251$; control vs. day 7 post-PHx $p = 0.0083$; **f**, Arginosuccinate: control, day 14 post-PHx $n = 4$; day 3 post-PHx, day 7 post-PHx $n = 5$; control vs. day 3 post-PHx $p = 0.0357$; **f**, Arginine: control, day 14 post-PHx $n = 4$; day 3 post-PHx, day 7 post-PHx $n = 5$; **f**, Ornithine: control, day 14 post-PHx $n = 4$; day 3 post-PHx, day 7 post-PHx $n = 5$; control vs. day 3 post-PHx $p = 0.0292$). The symbols '*'and '**' denote statistical significance at $p < 0.05$ and $p < 0.01$, respectively. Source data are provided as a Source Data File.

expressed. By resolving the tissue metabolites using MALDI imaging and mapping them against the functional liver zones described, we show de novo pyrimidine pathway metabolic flux along the defined functional zones of the liver tissue (Fig. 5d). This analysis, in tandem with the LC-MS and MALDI imaging data in Fig. 2d, e, and Fig. 4b shows accumulation of high levels of the orotate precursors, CA and DHO, in day 3 PHx mice treated with the DHODH inhibitor, but with spatial and fluxomic resolution. Of note, taurocholic acid (TCA) accumulates periportally, signifying precise mapping (Fig. 5d). This establishes applicability of the MALDI imaging method to functional spatial analysis of metabolic flux within liver tissue.

We applied this analysis to regenerating liver tissue following injection of $^{15}NH_4Cl$ and tracked the metabolic fluxes of labeled ammonia incorporation as it traverses the functional liver zones (Supplementary Fig. 7). Figure 5e illustrates the metabolic map of m + 0 and m + 1 isotopologues of pyrimidine precursors, zonally from periportal to pericentral in BAY-2402234-treated *vs.* untreated day 3 PHx and control livers. Detailed analyses show that higher levels of Glu and Gln in all PHx liver samples compared to controls are zonally distributed; whereas Glu is high periportally, Gln is high pericentrally (Fig. 5f). Interestingly, while Glu and Asp are higher in day 3 PHx liver compared to the control, treatment with the DHODH inhibitor shows accumulation of high levels of CA, coupled with combined reduction of Glu and Asp in the periportal zone (Fig. 5g), suggesting that Glu is transaminated to Asp and incorporated with CP to form CA within these zones. Notably, high levels of DHO accumulation are maintained along all liver zones in day 3 PHx liver treated with BAY-2402234 (Fig. 5h), indicating the availability of CA periportally and Gln pericentrally as DHO precursors, to facilitate de novo pyrimidine synthesis and, ultimately, supporting proliferation in the respective zones. Furthermore, the metabolic flux along the functional liver zones of m + 0 and m + 1 isotopologues are almost identical (Fig. 5e–h), demonstrating the incorporation of labeled ammonia into the respective de novo pyrimidine precursors spatially as they traverse the liver zones, as shown in Fig. 5a.

We applied a similar approach to regenerating liver after a more drastic resection by combined removal of left lateral and medial lobes, which equates to about ~ 60% PHx[17] (Fig. 6), and noted certain differences. The loss of body weight by about 2 g (assuming mouse weight of ~20 g), tantamount to the amount of tissue loss at ~ 60% PHx[17], did not fully recover to that of control mice at day 7 post-PHx (Fig. 6a), and is further reflected by the LBWR (Fig. 6b), suggesting an initial delay in regeneration possibly to make up for the bigger tissue loss. Although ~ 60% PHx mice treated daily with BAY-2402234 at 2 mg/kg have significantly reduced body weights and LBWR, the difference to untreated PHx mice only became significant from day 5 to day 7 post-PHx (Fig. 6a, b). EdU labeling revealed that despite an overall higher proliferative capacity (Figs. 1f, 6c), a significant proliferative difference can still be distinguished between treated and untreated mice on day 3 post-PHx (Fig. 6c) that is not reflected by body-weight and LBWR, suggesting effective attenuation of proliferation on day 3 post-PHx by BAY-2402234 when given at 2 mg/kg. Increasing the dose to 5 mg/kg however, while non-toxic to mice[18] (Supplementary Fig. 2), resulted to 67% mortality 2 days post-PHx (Supplementary Fig. 2), indicating that further suppression of DHODH by administering higher doses of BAY-2402234 at ~ 60% hepatic tissue loss increased mortality. Likewise, expression of the functional markers GLS2, CPS1 and GS showed very similar localization effectively mapping liver zonation as described where proliferation by EdU labelling spanned across periportal to pericentral zones (Fig. 6d). Similarly, BAY-2402234 treatment effectively attenuated DHODH as reflected by lower respiration (Fig. 6e), lower activity (Fig. 6f), and lower orotate to DHO ratio (Fig. 6g). More importantly, lower urea cycle activity is again evident following ~ 60% PHx from day 3 to day 7, as reflected by lower ratios of citrulline and CA (Fig. 6h), citrulline and ornithine (Fig. 6i), and blood urea levels (Fig. 6j).

When injected with $^{15}NH_4Cl$, labeled and unlabeled ammonia incorporated into de novo pyrimidine precursors similarly to ~ 35% PHx but accumulation of precursors, particularly Asp, Glu, CA, DHO, and orotate peaked earlier on day 3 post-PHx before tapering off on days 7 and 14 post-PHx (Fig. 4b and Supplementary Fig. 8a), suggesting earlier accumulation of precursors to support the higher proliferative capacity demonstrated by EdU labelling (Figs. 1f, 6c). In addition, we observed a 2-fold higher DHO accumulation upon treatment with BAY-2402234 on day 3 post-PHx (Fig. 4b and Supplementary Fig. 8a), suggesting that higher levels of precursors are being synthesized after ~ 60% PHx catering to increased proliferative capacity, and probably due to higher levels of ammonia processing as a consequence of greater tissue loss, as suggested by the isotope fraction enrichment data where up to ~75% of new CA and orotate stemmed from the labeled ammonia compared to only ~ 50% in ~ 35% PHx (Fig. 4c and Supplementary Fig. 8b). Interestingly, despite the same treatment with BAY-2402234 at 2 mg/kg for 3 days post-PHx, orotate accumulated 2-fold higher after ~ 60% PHx (Fig. 4b and Supplementary Fig. 8a), indicating 'attenuation' rather than 'suppression' of DHODH at the indicated dose after ~ 60% PHx, and hence, the significantly higher proliferation after ~ 60% PHx compared to ~35% PHx by EdU labelling in day 3 treated mice (Figs. 1f, 6c). Increasing the dose to 5 mg/kg, however, led to higher mortality (Supplementary Fig. 2).

When analyzed for the metabolic flux to show incorporation of ammonia into de novo pyrimidine precursors as it traverses the functional liver zones from periportal to pericentral 3 days post-PHx (Fig. 6k and Supplementary Fig. 9), incorporation into high levels of Glu and Gln showed periportal and pericentral accumulation, respectively (Fig. 6k, 6l). The high levels of Asp mirrored Glu with reducing trend from periportal to pericentral, indicative of the more periportal

https://doi.org/10.1038/s41467-025-65451-2

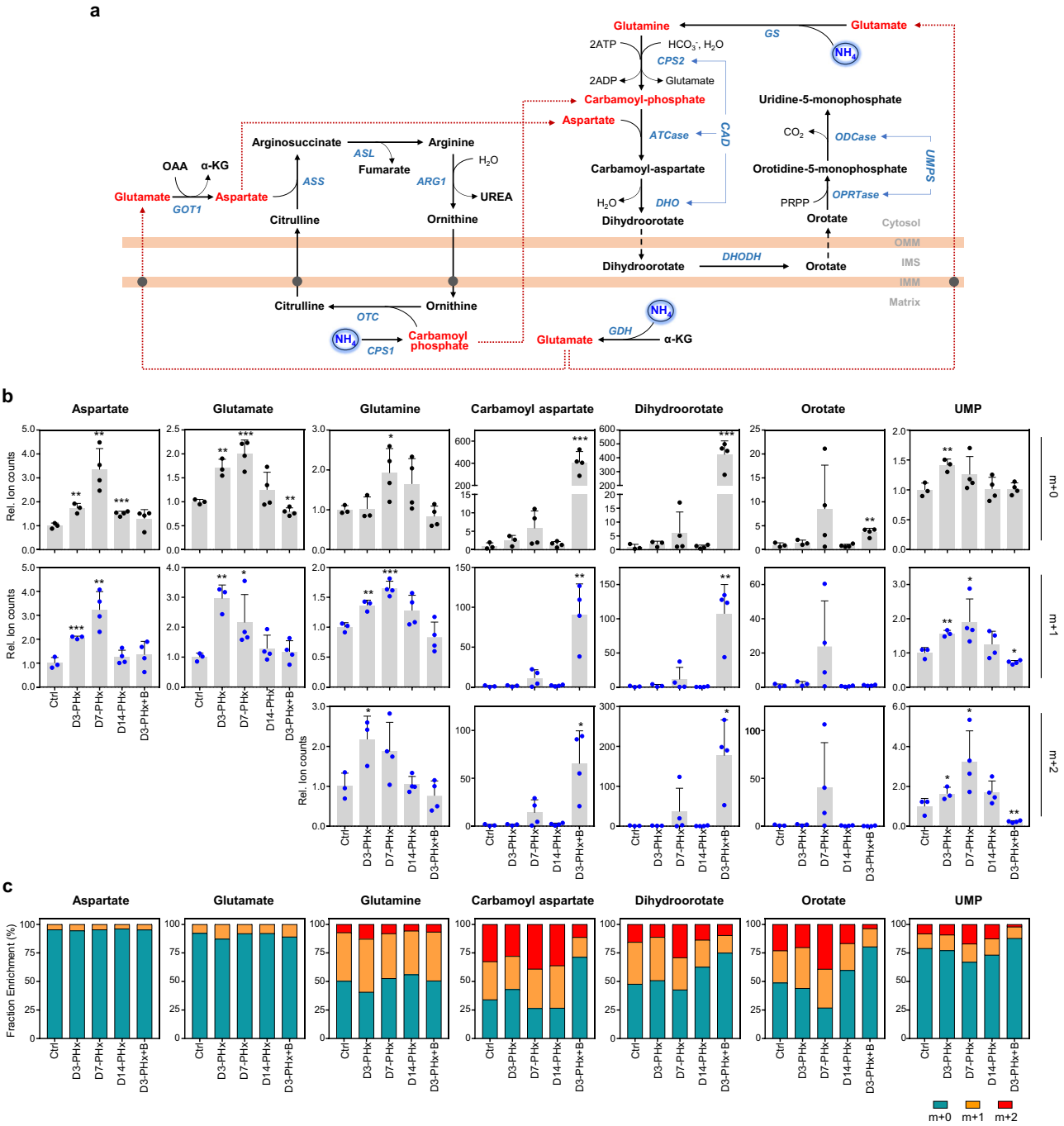

Fig. 4 | Ammonium is used by regenerating liver for anabolic processes. Scheme linking the urea cycle and the de novo pyrimidine pathway (**a**), showing the possible entry points of ammonia into the system and how they can be diverted and incorporated as de novo pyrimidine pathway precursors (red broken arrows; metabolites in red), and their m + 0, m + 1, and m + 2 isotopologue levels (**b**), analyzed by LC-MS using liver from $^{15}NH_4Cl$-injected control mice and from mice subjected to ~35% PHx with and without daily gavage of 2 mg/kg BAY-2402234 (BAY) at the indicated timepoints. **c** Isotope ratio reported as fraction enrichment (%) of all possible nitrogen isotope variations. For panel (**b**) unpaired *t* test was used and data are expressed as mean ± S.D. (For all m + 0, m + 1, and m + 2 isotopologues of metabolites: control, day 3 post-PHx $n = 3$; post-PHx days 7, 14, and 3 + 2 mg/kg BAY $n = 4$; m + 0 Aspartate: control vs. day 3 post-PHx $p = 0.0029$; control vs. day 7 post-PHx $p = 0.0032$; control vs. day 14 post-PHx $p = 0.0006$; m + 1 Aspartate: control vs. day 3 post-PHx $p = 0.0008$; control vs. day 7 post-PHx $p = 0.0025$; m + 0 Glutamate: control vs. day 3 post-PHx $p = 0.0014$; control vs. day 7 post-PHx $p = 0.0009$; control vs. day 3 post-PHx + 2 mg/kg BAY $p = 0.0062$; m + 1 Glutamate: control vs. day 3 post-PHx $p = 0.0010$; control vs. day 7 post-PHx $p = 0.0458$; m + 0 Glutamine: control vs. day 7 post-PHx $p = 0.0266$; m + 1 Glutamine: control vs. day 3 post-PHx $p = 0.0028$; control vs. day 7 post-PHx $p = 0.0003$; m + 2 Glutamine: control vs. day 3 post-PHx $p = 0.0193$; m + 0 Carbamoyl aspartate: control vs. day 3 post-PHx+2 mg/kg BAY $p = 0.0004$; m + 1 Carbamoyl aspartate: control vs. day 3 post-PHx +2 mg/kg BAY $p = 0.0053$; m + 2 Carbamoyl aspartate: control vs. day 3 post-PHx+2 mg/kg BAY $p = 0.0127$; m + 0 Dihydroorotate: control vs. day 3 post-PHx+2 mg/kg BAY $p = 0.0004$; m + 1 Dihydroorotate: control vs. day 3 post-PHx + 2 mg/kg BAY $p = 0.0042$; m + 2 Dihydroorotate: control vs. day 3 post-PHx + 2 mg/kg BAY $p = 0.0106$; m + 0 Orotate: control vs. day 3 post-PHx + 2 mg/kg BAY $p = 0.0022$; m + 0 UMP: control vs. day 3 post-PHx $p = 0.0049$; m + 1 UMP: control vs. day 3 post-PHx $p = 0.0029$; control vs. day 7 post-PHx $p = 0.0383$; control vs. day 3 post-PHx+2 mg/kg BAY $p = 0.0101$; m + 2 UMP: control vs. day 3 post-PHx $p = 0.0493$; control vs. day 7 post-PHx $p = 0.0299$; control vs. day 3 post-PHx + 2 mg/kg BAY $p = 0.0059$). The symbols '*', '**', and '***' denote statistical significance at $p < 0.05$, $p < 0.01$, and $p < 0.001$, respectively. Source data are provided as a Source Data File.

https://doi.org/10.1038/s41467-025-65451-2

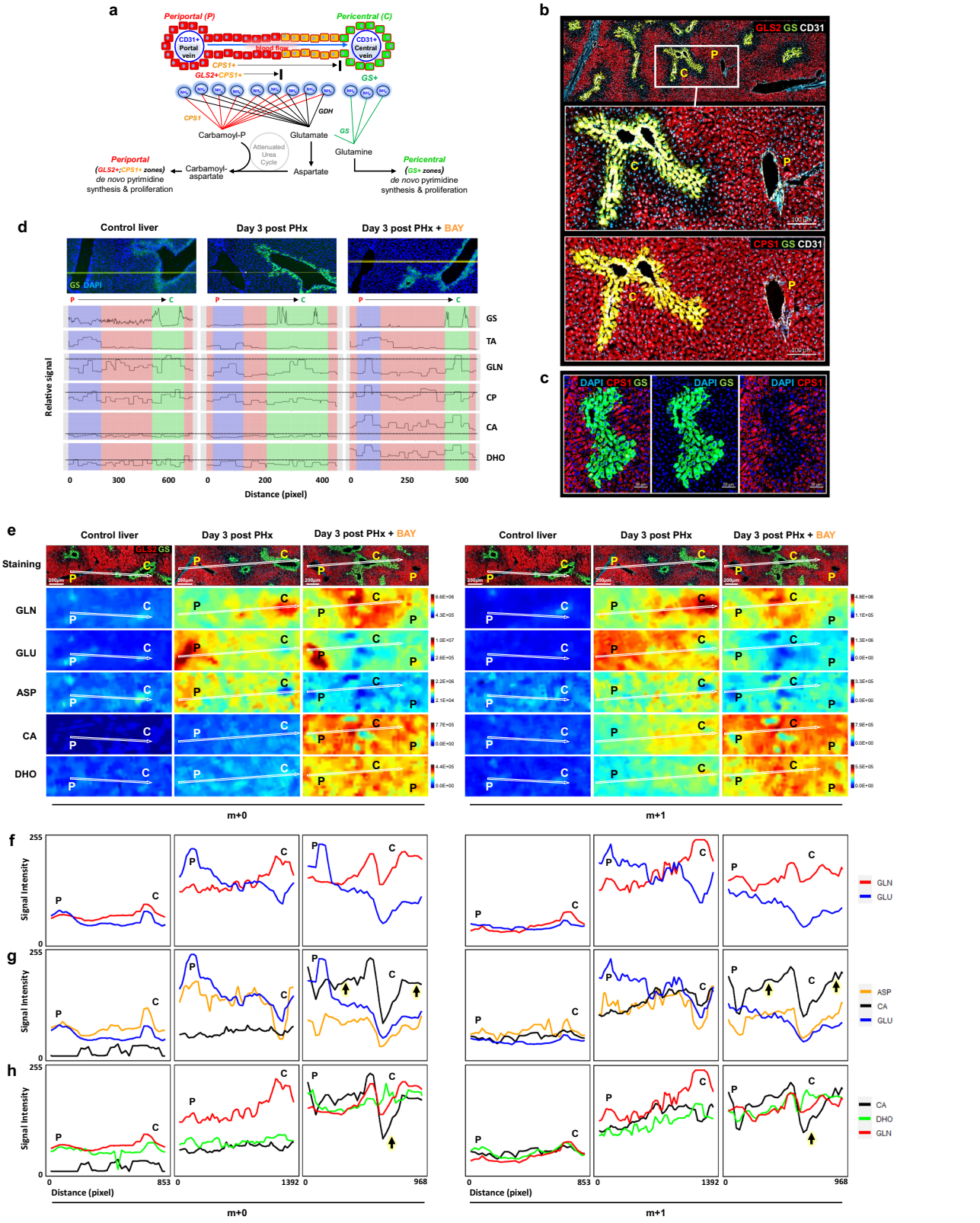

urea cycle activity incorporating ammonia into Glu, then transaminating to Asp (Fig. 6k, m). Interestingly, treatment with BAY-2402234 led to near depletion of Gln levels not observed in ~ 35% PHx (Figs. 5e, f, 6k, l), whose flux mirrors a concurrent higher level of the orotate precursors Asp, CA, and DHO peaking at the highest pericentrally (Fig. 6k, m, n). This suggests that under conditions of greater hepatic tissue loss (~ 60% PHx), a more active pericentral incorporation of ammonia into de novo pyrimidine precursors occurs. The almost identical flux exhibited by $^{15}NH_4Cl$ into the respective m + 1 isotopologues confirms ammonia incorporation into the respective de novo pyrimidine precursors as it traverses the functional liver zones (Fig. 6k–n).

Fig. 5 | Liver regeneration involves zoning of metabolic pathways. a Scheme of functional liver zonation into glutaminase-2 positive (GLS2 +) periportal (P), carbamoyl phosphate synthase positive (CPS1 +) periportal (P) extending towards but mutually exclusive to glutamine synthetase positive (GS +) pericentral (C) regions depicting how ammonia is 'scavenged' and incorporated into the de novo pyrimidine pathway spatially within a regenerating liver as it traverses the respective zones towards the direction of blood flow as indicated. The respective zones described are imaged in the mouse liver (**b**), showing periportal (P) to pericentral (C) staining using the functional markers GLS2 and GS, respectively, with the endothelium lining the blood vessels positive for CD31, and with the GS+ zone mutually exclusive with the CPS1 + zone (**c**). **d** Combined analyses using imaging to depict liver functional zones (upper panel) in tandem with MALDI-TOF analysis (lower panels) on the same zones (depicted by yellow line in imaging panels) using liver of control mice and mice subjected to ~ 35% PHx with or without daily gavage of 2 mg/kg BAY-2402234, showing metabolic fluxes of de novo pyrimidine metabolites from periportal (P) to pericentral (C) zones (arrows). Horizontal bars on lower panels represent metabolic flux set relative to control levels. Taurocholic acid (TCA) and GS staining were used to demarcate periportal and pericentral zones, respectively. **e** Similar combined analyses using imaging to identify liver functional zones as previously described using specific markers (upper panel) in combination with MALDI-FTICR (lower panels) in liver taken from $^{15}NH_4Cl$-injected control mice and from mice subjected to ~ 35% PHx with and without daily gavage of 2 mg/kg BAY-2402234 showing distribution of m + 0 and m + 1 isotopologues of de novo pyrimidine precursor metabolites that can incorporate ammonia within the functional liver zones. Using MALDI-FTICR data on the functional zones identified through imaging (depicted by white arrow from P to C on upper panel of **e**), the periportal (P) to pericentral (C) m + 0 and m + 1 metabolic fluxes of isotopologues of pyrimidine precursors that can potentially incorporate ammonia, specifically Gln and Glu (**f**), CA, Asp and Glu (**g**; arrows point to the 'P' zone), and DHO and its upstream substrates Gln and CA (**h**; arrows point to the 'C' zone), are shown. MALDI-TOF and MALDI-FTICR images were acquired with the 9AA and DAN matrices measured in the negative mode, respectively. Images are displayed with TIC normalization (MALDI-TOF) or RMS normalization (MALDI-FTICR), 99% quantile hotspot removal, linear interpolation and weak denoising level. Peak intensities rescaled to full color map. Source data are provided as a Source Data File.

Notably, non-surgical naïve and surgical unhepatectomized sham mice with and without BAY-2402234 treatment when used as controls, demonstrated that surgery and BAY-2402234 treatment itself did not compromise overall health of mice at the time of experimental measurements (Fig. 6a). In addition, when isotope fraction enrichment data were analyzed using intensities of the MALDI-FTICR imaging for ~35% PHx (Supplementary Fig. 7) and ~ 60% PHx (Supplementary Fig. 9), similar to LC-MS data (Figs. 3g, 4c and Supplementary Fig. 8b), a tendency to a more upstream processing of new intermediates in the urea cycle indicate ammonia redirection to new pyrimidine precursors Gln, CA, DHO, and orotate in the de novo pyrimidine pathway (Supplementary Fig. 10a, b). Intriguingly, the tissue levels of BAY-2402234 correlated positively with CA and DHO, and negatively with orotate and UMP in a timepoint-dependent manner from day 3 to 7 to 14 post ~ 60% PHx (Supplementary Fig. 11a, b), where BAY-2402234 at 2 mg/kg only attenuates rather than suppress liver regeneration (Fig. 4b, Supplementary Fig. 8a and Figs. 1f, 6c). This suggests that its effect on DHODH inhibition is not only dependent on its levels in the tissue, but also on the extent of liver regeneration (albeit attenuated in this case), where a more 'normalized' liver on days 7–14 compared to day 3 post-PHx, is better able to presumably metabolize the drug, lowering its levels, hence its effects (Supplementary Fig. 11a, b).

Discussion

Of the various tissues, the liver is endowed with the exceptional feature of regeneration, and up to 90% PHx still allows for complete re-growth of the organ[1–3]. This process involves rapid liver volume increase post-PHx due to CCH, followed by very fast proliferation of hepatocytes such that the number of cells in the regenerating liver within 7 days is similar to that of the pre-PHx organ[5,6,22]. This intriguing 'memory' within the liver is particularly noteworthy. Moreover, it holds significant implications for liver transplantation, where matching of the original liver size given by cell number is imperative for its function, supporting a strictly regulated process[23].

The highly robust proliferation of hepatocytes after PHx is accompanied by activation of anabolic pathways that support liver cell proliferation[7–10]. While there is relatively good knowledge about the various pathways that are upregulated and downregulated in the regenerating liver, with mitochondria being an important player in these pathways[7,23], virtually nothing is known about the possible role of the de novo pyrimidine pathway in liver regeneration. To the best of our knowledge, there are only a few reports focusing on the formation of nucleotides, often in cultured cells, including hepatocytes[24–26]. This is surprising given the fact that rapidly proliferating cells, typically represented by cancer cells, need de novo pyrimidine synthesis to support rapid transition through the S-phase of the cell cycle, and that DHODH, the 'mitochondrial component' of the pathway, is a vulnerability that can be exploited for cancer treatment[27–29]. Further, it was shown that DHODH is expressed early in malignant transformation, most likely to support rapid cell proliferation[30]. Our own research has shown that the de novo pyrimidine pathway is linked to horizontal mitochondrial transfer in the context of tumor formation and progression, supporting the requirement of this pathway for rapid cell proliferation[14–16].

Linked to the above, we reasoned that due to very high proliferation rates, regenerating liver after ~ 35% PHx is likely to be dependent on the de novo pyrimidine pathway. Indeed, we show here that this is the case. Our first evidence is based on the use of a highly specific inhibitor of DHODH, the enzyme that catalyzes the fourth reaction of the pathway. We show that the inhibitor suppresses cell proliferation in the liver after ~ 35% PHx by inhibiting DHODH-dependent respiration and DHODH activity. This clearly points to the importance of DHODH activity, and consequently, DHODH-dependent respiration in liver regeneration. We next investigated the metabolomics of the de novo pyrimidine pathway and, consistent with the above-mentioned results, we found that DHODH inhibition caused high-level accumulation of DHO, as shown earlier in the context of cancer[16,18], as well as that of CA.

Since regenerating liver has a high demand for pyrimidines to support robust cell proliferation of the tissue, we investigated the origin of substrates for de novo pyrimidine synthesis that should be formed in higher amounts to comply with the anabolic needs of regenerating liver. The 'classical' substrate for the pathway is Gln. In the context of the functional liver histology, this may hold true pericentrally, where GS is expressed in abundance. However, the periportal presence of high levels of GLS2, whose primary function is to break down Gln into Glu and ammonia, with the latter known to further stimulate GLS2 as an amplification loop for the urea cycle[31], presents a dichotomous scenario. With this in mind, by using functional spatial metabolomics in regenerating liver with perceived urea cycle attenuation, we present an interesting concept where two of its main substrates, CP catalyzed by CPS1, and Asp from transamination of Glu, both metabolically capable of scavenging ammonia in the periportal parenchyma, are redirected as de novo pyrimidine precursors where, histologically, Gln is not available. As proliferation in regenerating liver is disproportionately high in the combined periportal and parenchymal regions outside the bounds of the pericentral zone, the urea cycle attenuation presents a major hepatic metabolic remodeling event to support increased demand for pyrimidines, where, based on functional histology, Gln is not directly available as a substrate. This zonal nature of metabolic remodeling, where the periportal/parenchymal urea cycle metabolic flux is redirected towards the de novo

https://doi.org/10.1038/s41467-025-65451-2

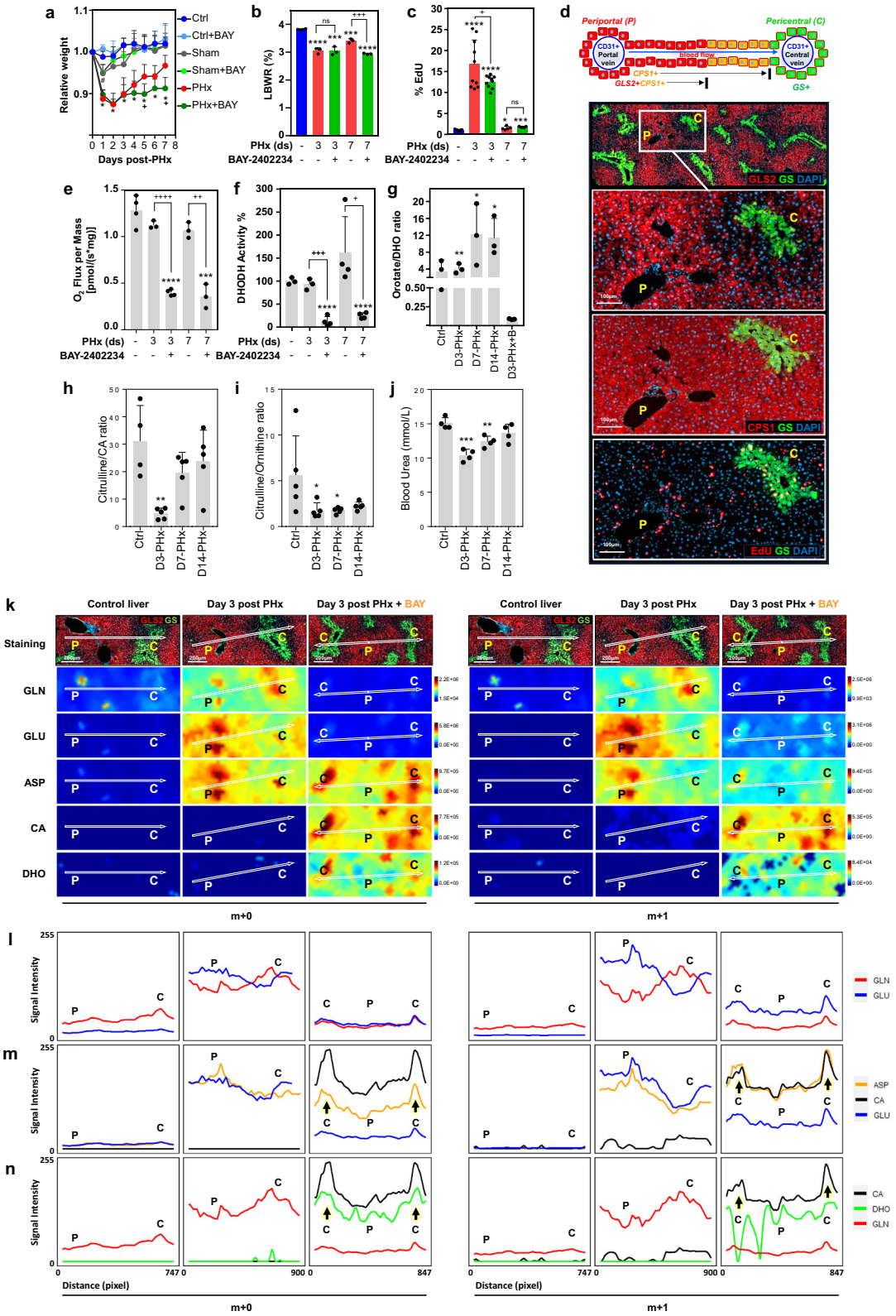

pyrimidine synthesis when the demand for proliferation is high, is a concept supported by our data. Of note, similar functional consequences of attenuated urea cycle activity in pathological disorders, albeit irreversible, have been documented[32]. Furthermore, the fact that ammonia detoxification by the urea pathway, facilitated by CPS1, is strictly periportal[33] gives credence to the zonal metabolic remodeling events we observed during liver regeneration, though in a reversible manner.

Ammonia detoxification is a major liver function facilitated by the urea cycle. Tracing analysis of urea cycle metabolites, using ammonia with a stable isotope of nitrogen, shows low levels of metabolites of the urea cycle in regenerating liver as well as low activity of the pathway, given by the ratio of citrulline to CA. We also found that the activity of the first step of the urea cycle, catalyzed by OTC, is diminished in the regenerating liver. This attenuation, coupled with the reduced liver capacity by up to ~ 60% due to resection, poses a possible problem

Fig. 6 | Regenerating liver after ~ 60% partial hepatectomy has attenuated urea cycle with exacerbated pericentral ammonium use for de novo pyrimidine synthesis. Relative body weight (**a**), liver/body weight ratio (LBWR, %) (**b**), and assessment of proliferation by EdU assay (**c**) in control mice and mice subjected to ~ 60% PHx, with or without daily gavage of 2 mg/kg of BAY-2402234 (BAY) and sham-operated mice as indicated. **d** Localization of EdU+ cells within the functional liver zones imaged by GLS2+ periportal (P) and CPS1 + zones extending towards a mutually exclusive GS+ pericentral zone (C). Assessments of DHODH-dependent respiration (**e**), DHODH activity (**f**), orotate-to-DHO ratio (**g**), urea cycle activity as a ratio of citrulline and carbamoyl aspartate (CA) (**h**), as a ratio of citrulline and ornithine (OTC activity) (**i**), and as blood urea levels (**j**), in control mice and mice subjected to ~ 60% PHx with or without daily gavage of 2 mg/kg BAY. **k** Combined analyses by liver functional zone imaging as described using specific markers (upper panel) in combination with MALDI-FTICR images (lower panels) of liver taken from $^{15}NH_4Cl$-injected control mice and from mice subjected to ~ 60% PHx with and without daily gavage of 2 mg/kg BAY showing distribution of m + 0 and m + 1 isotopologues of de novo pyrimidine precursor metabolites that can incorporate ammonia within the functional liver zones. Using MALDI imaging data on the functional zones identified through imaging (depicted by white arrow from P to C on upper panel of **k**), the periportal (P) to pericentral (C) m + 0 and m + 1 metabolic fluxes of isotopologues of pyrimidine precursors that can potentially incorporate ammonia, specifically Gln and Glu (**l**), CA, Asp and Glu (**m**; arrows point to the 'C' zone), and DHO and its upstream substrates Gln and CA (**n**; arrows point to the 'C' zone), are shown. MALDI-FTICR images were acquired with the DAN matrix and measured in the negative mode. Images are displayed with RMS normalization, 99% quantile hotspot removal, linear interpolation and weak denoising level. Peak intensities rescaled to full colormap. For panel (**a**) multiple *t* tests using the Holm-Sidak method were used (control $n = 5$, control + BAY $n = 4$, sham $n = 8$, sham + BAY $n = 8$, PHx $n = 10$, PHx + BAY $n = 13$; control vs. day 1 sham $p = 0.0196$; control vs. day 1 sham+BAY $p = 0.0205$; *p*-values for control vs. PHx at days 1, 2, 3, 4, 5, 6 and 7 post-PHx are 0.000002, 0.00000005, 0.0001, 0.0004, 0.0010, 0.0002, and 0.0010, respectively; *p*-values for control vs. PHx + BAY at days 1, 2, 3, 4, 5, 6 and 7 post-PHx are 0.000000001, 0.0000009, 0.0000003, 0.00002, 0.00002, 0.000009, and 0.00001, respectively; *p*-values for PHx vs. PHx+BAY at days 5 and 7 post-PHx are 0.0278 and 0.0025, respectively). For panels (**b**, **c**), and (**e**–**j**), unpaired *t* test was used (**b**: control $n = 4$, days 3 and 7 ± BAY $n = 3$; *p*-values for control vs. post-PHx at days 3, 3 + BAY, 7, 7 + BAY are < 0.0001, 0.0001, 0.0001, and < 0.0001, respectively; day 7 post-PHx vs. day 7 post-PHx+BAY $p = 0.0005$; **c**: control $n = 5$, day 3 post-PHx ±BAY $n = 10$, day 7 post-PHx ± BAY $n = 5$; *p*-values for control vs. post-PHx days 3, 3 + BAY, 7, 7 + BAY are < 0.0001, < 0.0001, 0.0475, and 0.0002, respectively; day 3 post-PHx vs. day 3 post-PHx+BAY $p = 0.0407$; **e**: control $n = 4$, day 3 post-PHx $n = 3$, day 3 post-PHx+BAY $n = 4$, day 7 post-PHx ±BAY $n = 3$; control vs. day 3 post-PHx +BAY $p = <0.0001$; control vs. day 7 post-PHx+BAY $p = 0.0005$; day 3 post-PHx vs. day 3 post-PHx+BAY $p < 0.0001$; day 7 post-PHx vs. day 7 post-PHx + BAY $p = 0.0014$; **f**: control $n = 3$, day 3 post-PHx $n = 3$, day 3 post-PHx + BAY $n = 4$, day 7 post-PHx ± BAY $n = 4$; control vs. day 3 and 7 post-PHx+BAY p < 0.0001; day 3 post-PHx vs. day 3 post-PHx+BAY $p = 0.0002$; day 7 post-PHx vs. day 7 post-PHx + BAY $p = 0.0123$; **g**: all groups $n = 3$; *p*- values of day 3 post-PHx + BAY vs. post-PHx days 3,7, and 14 are 0.0037, 0.0462 and 0.0140, respectively; **h**: control $n = 4$; days 3, 7, and 14 post-PHx $n = 5$; control vs. day 3 post-PHx $p = 0.0013$; **i**: all groups $n = 5$; control vs. day 3 post-PHx $p = 0.0408$; control vs. day 7 post-PHx $p = 0.0390$; **j**: all groups $n = 4$; control vs. day 3 post-PHx $p = 0.0001$; control vs. day 3 post-PHx $p = 0.0001$; control vs. day 7 post-PHx $p = 0.0019$). Data are expressed as mean ± S.D. The symbols '*/+', '**/++', '***/+++', and '****/++++' denote statistical significance at $p < 0.05$, $p < 0.01$, $p < 0.001$, and $p < 0.0001$, respectively; ns, not significant. Source data are provided as a Source Data File.

concerning the metabolic fate of ammonia. Interestingly, we found that the urea cycle's ammonia-scavenging mechanism via Glu and Asp, as well as its incorporation into carbamoyl phosphate mediated by CPS1, works in tandem with pericentral GS in diverting ammonia as anabolic pyrimidine precursors in their respective functional zones (see scheme in Fig. 5a). Even more intriguing is the proportionate increase in the capacity to divert ammonia into pyrimidine precursors when the need for proliferation is further enhanced, as reflected by the exacerbated hepatic tissue loss upon ~ 60% liver resection, where not only was proliferative capacity increased, but a proportional increase in ammonia-derived pyrimidine precursors was also noted. In particular, the increase in Gln-derived pyrimidine precursors fluxing pericentrally provides evidence of higher levels of ammonia flowing through the functional liver zones, mainly because anatomically, the central vein is the liver's exit point towards systemic circulation, and it is in the central veins where GS+ cells synthesize Gln from ammonia.

The greater loss of hepatic tissue in this case presumably leads to an even greater acute increase in ammonia levels that need to be processed to prevent toxicity. Under this circumstance, the importance of a functional de novo pyrimidine pathway via DHODH along the functional zones in the regenerating liver cannot be further emphasized, as not only does it provide for the anabolic requirement for hyperactive liver regrowth, but it also helps 'detoxify' ammonia via diversion when urea production is low, hence increasing mortality when its function is blocked. The use of a toxic product, ammonia, being utilized for anabolic processes, implies a counterintuitive scenario. Support for this idea comes from recent work, which showed that ammonia is used in the liver to form Glu from α-KG and Gln from Glu, both of which are then used for biomass build-up for rapidly proliferating cancer cells[34]. In addition, it has been shown that reduced activity of enzymes of the urea cycle diverts ammonia in both cancer and urea cycle deficiency syndromes, to support de novo pyrimidine synthesis[35–38].

Surprisingly, not much is known about altered activity of the urea cycle in the context of liver regeneration, although there is an earlier paper on the possible role of salvage and de novo pathways of nucleotides; however, no definitive conclusion was reached[39], including the potential use of ammonia and its role in the process. To link the lower urea cycle activity and the use of ammonia for generating pyrimidine precursors, similar to that shown for breast cancer[34,40], we traced stable isotopes of the de novo pyrimidine pathway following injection of labeled ammonium chloride. This analysis confirmed that ammonia that is not detoxified in the regenerating liver is used for generating CA, converted from CP and Glu and Asp periportally, and Gln pericentrally, and used as substrates for de novo pyrimidine synthesis to effect liver regrowth. The relevance of the urea cycle in ammonia diversion is further highlighted in a study in pancreatic cancer, where CPS1 was shown to redirect CP towards de novo pyrimidine synthesis by utilizing it as a substrate for the second catalytic activity of CAD, aspartate carbamoyl transferase-2 (ACT2)[41]. The plausibility of these scenarios occurring in liver regeneration is given by our results showing the presence of m + 0 and m + 1 isotopologues of CA and DHO in regenerating liver and its accumulation upon treatment of the regenerating tissue with BAY-2402234. Using a MALDI imaging approach, we were also able to spatially resolve metabolites of the de novo pyrimidine pathway, in particular by showing that formation of Glu and its flux towards Asp and CA was mainly in the periportal regions where the urea cycle is localized, and Gln mainly pericentral. The downstream metabolic flux, supporting de novo pyrimidine synthesis, is largely confined to respective regions upon BAY-2402234 treatment, highlighted by the periportal to pericentral differential accumulation of Glu and Gln.

The importance of our finding of metabolic remodeling, resulting in higher levels of pyrimidine precursors, is underscored by evidence that some of these substrates are shared with other anabolic pathways, such as de novo purine and amino acid synthesis pathways[34,40]. Our findings also have clinical relevance, which is linked to increased levels of ammonia. This occurs in certain pathologies, in particular those with a dysfunctional urea cycle, resulting in hyperammonemia presenting with toxic effects of ammonia that can no longer be detoxified in the liver due to deficiency or mutations of genes coding for urea cycle enzymes[37,42]. Of these, the OTC gene is affected most frequently[38]. Thus, under these pathological conditions, ammonia is a highly toxic substance with severe neurological consequences. On the other hand,

in the regenerating liver following PHx, which is a frequent approach to the management of liver diseases, ammonia plays a positive role, being used for anabolic processes that are needed for liver regeneration. This shows that ammonia can be highly toxic or beneficial in mammals, a feature that is context-dependent.

In conclusion, we show that liver regeneration requires de novo synthesis of pyrimidines and that this is made possible by the use of ammonia from the less active urea cycle to generate the necessary pyrimidine precursors in functionally relevant liver zones. We also show the pathway changes after PHx to support the anabolic de novo pyrimidine pathway, and a 'switch' back towards homeostasis upon completion of liver regeneration. Probably the most intriguing aspect of this research is that our results point to the use of a toxic byproduct, which is normally converted to urea and excreted, for tissue regeneration.

Methods

Ethical statement

This research complies with all relevant ethical regulations. All animal work was approved by the Ethics Committee of the Institute of Molecular Genetics, Prague (permit number 120-2024-P) in accordance with the Czech guidelines for the Care and Use of Animals in Research and Teaching and the Animal Protection Law of the Czech Republic.

Animal Work

For all animal studies, 12–14 weeks old female C57BL/6 J mice (randomized in groups; inbred house strain in the Czech Centre for Phenogenomics, Prague, Czech Republic), kept at specific pathogen-free condition under a light regime of 12/12 h, maintained at 20–23 °C with relative humidity of 45–65%, and with free access to water and food (Altromin, cat# 1324), were used. To reduce variability associated with sex-related biological differences, only female mice were used. To induce liver regeneration by partial hepatectomy, mice were anesthetized using isoflurane (2%, 2 l/min O_2 flow rate) and the liver exposed by making an upper midline incision starting from the xiphoid process, then extended to 2 cm caudally. The left lateral lobe (LLL), representing ~ 35% of the liver, or the left lateral lobe with the median lobe (ML), representing ~ 60% of the liver[17], were ligated, excised, and the incision closed using 5–0 polydioxanone (PDS II, Ethicon) suture. Following partial hepatectomy, body weight and survival were monitored daily.

To treat mice with the dihydroorotate dehydrogenase (DHODH) inhibitor, BAY-2402234 (MedChemExpress, HY-112645) was dissolved in DMSO (Sigma, D2650) at 5.2 mg/ml, reconstituted in corn oil (Sigma, D8267) at the final concentration of 0.2 mg/ml, and administered in mice by daily oral gavage at 2 or 5 mg/kg. Alanine transaminase (ALT), aspartate transaminase (AST), and blood urea nitrogen (BUN) levels were measured using a biochemical analyzer (Beckman Colter AU480). To label proliferating hepatocytes with 5-ethynyl-2-deoxyuridine (EdU, MedChemExpress, HY-118411) in vivo, mice were intraperitoneally injected with 50 mg/kg EdU in phosphate-buffered saline (PBS) 6 h before sacrifice. To treat mice with labeled ammonium chloride ($^{15}NH_4Cl$) (Sigma, 299251) for metabolic tracing analysis, mice were intraperitoneally injected with 9 mmol/kg $^{15}NH_4Cl$ in physiological saline 30 min before sacrifice. For isotypic control in MALDI-FTICR experiments, non-labeled ammonium chloride (NH_4Cl) (Sigma, A4514) was used in mice as described. For the specific *n* number of mice used, please refer to the Source Data file and main figure legends.

Liver Collection

Mice were sacrificed by anesthetic overdose with isoflurane. The right inferior liver lobes were collected and snap-frozen in liquid nitrogen, and kept as fresh frozen samples at -80 °C. The right superior liver lobes were collected and washed serially in pre-warmed 2 and 10% (w/w) gelatin solution, respectively. The samples were then transferred to cryomolds with fresh 10% gelatin solution and flash-frozen in the Novec 7200 bath (3 M) tempered in liquid nitrogen, and subsequently stored at -80 °C prior to cryosectioning.

Cryosectioning

Frozen tissue blocks were cooled to -12 °C in the CM1950 cryostat (Leica Biosystems) and cut in random order to 10 μm thick sections. Cryosections were mounted onto warm ITO glass slides (Ossila, UK) for matrix-assisted laser desorption/ionization mass spectrometry imaging (MALDI MSI) analyses. Corresponding consecutive cryosections were also collected and mounted onto Superfrost plus glass slides (Thermo Fisher Scientific) for immunofluorescence (IF) staining. All tissue sections were dried in a desiccator for 15 min, packed in plastic slide mailers, and vacuum-sealed for storage at -80 °C until MALDI imaging and IF staining.

Tissue slide preparation for MALDI imaging

Tissue sections were removed from the freezer and adjusted to room temperature for 30 min, and placed in a desiccator for 15 mins to dry. For measurements using the MALDI-Time-of-Flight (TOF) imaging platform, 9-aminoacridine (9AA; Sigma,92817) at 10 mg/ml in 70% ethanol (v/v) was sprayed onto tissue sections in 12 matrix layers using the following parameters: spray nozzle temperature, 50 °C; flow rate, 35 μl/min; horizontal nozzle movement speed, 1000 mm/min; nitrogen flow rate, 2 l/min; gas pressure, 10 psi; distance between each pass, 2 mm; nozzle distance, 42 mm. The same sample preparation method, except the flow rate adjusted to 50 μl/min, was used for phosphate group-containing metabolite profiling using the MALDI- Fourier transform ion cyclotron resonance (FTICR) mass spectrometry (MS). For general metabolite profiling using the MALDI-FTICR MSI, 1,5-diaminonaphthalene (DAN; Sigma, 56451) at 10 mg/ml in 70% acetonitrile (v/v) was sprayed onto tissue sections in 10 matrix layers using a pneumatic sprayer (TM-Sprayer 3, HTX Imaging) according to the following parameters: spray nozzle temperature, 65 °C; flow rate, 50 μl/min; horizontal nozzle movement speed, 1000 mm/min; nitrogen flow rate, 2 l/min; gas pressure, 10 psi; distance between each pass, 2 mm; nozzle distance, 42 mm. Prior to MALDI imaging, matrix-layered tissue sections were placed in a desiccator for at least 30 min.

MALDI imaging measurement

MALDI-TOF spectra of 3 biological replicates for a control (Ctrl) group, 3 days post ~35% PHx (D3-PHx) group, and 3 days post ~ 35% PHx with BAY-2402234 treatment (D3-PHx + B) group (9 in total) were acquired in sets of 3 (representing an experimental cohort where each group is represented per acquisition) using the rapifleX MALDI-TOF/TOF mass spectrometer (Bruker Daltonics) operated by the fleXcontrol v4.2 software (Bruker Daltonics) in the reflector negative-ion mode with the 355 nm SmartBeam™ 3D laser (spatial resolution of 50 × 50 μm, m/z range of 20–1000) at the constant laser fluence of 88% and laser frequency of 5 kHz. 200 shots were summed up from each position. The instruments were set up accordingly: ion source 1, 19.973 kV; PIE, 2.664 kV; lens, 11.353 kV; reflector 1, 20.810 kV; reflector 2, 1.034 kV; reflector 3, 8.577 kV. The pulsed ion extraction time was set to 90 ns, detector gain was 2302 V. Data were acquired with a digitizer speed at 2.5 GS/s. Calibration was done externally using red phosphorus to achieve precision up to 2 ppm[43]. Spatial navigation for imaging data acquisition was done in the flexImaging v6.0 software (Bruker Daltonics).

MALDI-FTICR imaging experiments on a representative biological sample per experimental group (3 in total) from mice treated with $^{15}NH_4Cl$ were conducted in the negative ion mode using the MALDI-solariX 12T-2ω Fourier transform ion cyclotron resonance (FTICR) mass spectrometer (Bruker Daltonics) equipped with the Smartbeam II 2 kHz laser, and operated by the ftmsControl v2.3.0 software. The laser

focus was selected to achieve a lateral resolution of 35 × 35 µm by summing up 100 laser shots at the 1 kHz laser frequency and constant laser power. The instrument parameters were adjusted to maximize ion intensities of compounds of interest, considering the sample preparation, including the MALDI matrix. First, for samples overlaid with the DAN matrix, data were collected in the mass range of 40–650 *m/z* with one acquired spectrum per pixel. The data were collected with 2 M data points in the transient (0.21 s), which provided the estimated resolving power of 48,000 at *m/z* of 400. The ion optic parameters were optimized to maximize ion transmission within the defined *m/z* range, including the funnel RF amplitude (80 Vpp), collision cell (collision voltage: 1.5 V, DC bias: -1.0 V), time-of-flight delay (0.4 ms), and transfer optics (6 MHz, Q1 *m/z* 100). Second, the MALDI MSI method used for the samples prepared with the 9-AA matrix was adjusted as follows. MS data were acquired in the mass range of 100–650 *m/z* and continuous accumulation of selected ions mode, allowing for a selection of multiple mass windows, including one isolation window of 70 Da with the Q1 mass of 130 *m/z*, and the second isolation window of 300 Da with the Q1 mass of 380 *m/z*. The parameters of ion transfer optics were kept the same as used in the above-mentioned MALDI-FTICR MSI method except for the Q1 mass. Data were acquired with 2 M data points in the transient (0.56 s), providing an estimated resolving power of 130,000 at *m/z* 400. Both MSI methods were externally calibrated on clusters of red phosphorus prior to data acquisition, achieving mass accuracy better than 1 ppm[43]. Spatial navigation for imaging data acquisition was set in the flexImaging v5.0 software (Bruker).

Tissue from the right inferior liver lobes after ~60% hepatectomy, previously chopped into 1 mm^3 pieces, was transferred to 2 ml Eppendorf tube, weighed, and methanol/acetonitrile/water (4:4:2, v/v) was added at the ratio of 20 µl per mg of tissue. One stainless steel ball was added to each tube, and tissue was immediately homogenized in TissueLyser II (QIAGEN) for 2 min at 30×s^{-1} frequency at room temperature. Samples were then transferred to -20 °C and left to precipitate overnight. The next day, the samples were spun down in a centrifuge cooled to 4°C at 20,000 × *g* for 5min. 1 µl of the supernatant was mixed with 9 µl of the DAN matrix solution (10 mg/ml in 70% acetonitrile). 0.5 µl of the sample-matrix mixture was spotted onto a stainless steel MALDI target and dried. Pure reference standards (DL-aspartic acid, Sigma, A9006; L-citrulline, Merck, PHR3191; L-glutamic acid monosodium salt monohydrate, Sigma, 49621; L-glutamine, Merck, G5792; orotic acid, Sigma, O2750; dihydroorotic acid, Sigma, D7128; L-ornithine monohydrochloride, Merck, 57197; N-carbamoyl-DL aspartic acid, TCI EUROPE N.V., C0029; uridine 5′-monophosphate, Sigma, U1752; BAY-2402234, MedChemExpress, HY-112645) were dissolved in methanol/acetonitrile/water (4:4:2, v/v/v) at concentrations of 1 mM. 1 µl of the standard solution was mixed with 9 µl of the DAN matrix solution (10 mg/ml in 70% acetonitrile), and 0.5 µl of the standard-matrix mixture was spotted onto stainless steel MALDI target and dried. The metabolites of interest were identified by the fragmentation experiments using the MALDI-FTICR MS/MS analysis in the negative ion mode. MS/MS data were acquired in the mass range of 50–650 m/z with external mass calibration to ion clusters of red phosphorus before data acquisition, and with a resolving power of 150,000 at *m/z* 150. The product ion mass spectra of $[M\text{-}H]^-$ precursor ions were acquired with the smartbeam laser operated at 1 kHz laser frequency with 100 laser shots per position. The precursor ions were isolated in the quadrupole with the isolation window of 1 Da and fragmented via collision-induced dissociation applying optimized collision energy (5 V) for each measured molecular ion, e.g., aspartate, citrulline, glutamine, glutamate, orotate, uridine 5′-monophosphate, dihydroorotate, carbamoylaspartate, uridine, and ornithine. The acquired MALDI MS/MS spectra were averaged by summing 16 to 32 scans from each sample (Supplementary Fig. 12). Spectra similarity score was assessed using the mzCloud standalone application (www.mzcloud.org) (Supplementary Table 1).

MALDI imaging data processing

Raw data files generated by the TOF and FTICR instruments were imported as full spectra into SCiLS Pro software v2025b Pro (Bruker Daltonics). Spectra from TOF measurements were normalized by the total ion current method (TIC), while spectra from the FTICR instrument were normalized using the root mean square method (RMS). Intensity at peak maximum was reported in both cases using the rainbow color map. Images were displayed with linear interpolation, and the image denoising level was set to “weak”. The hotspot removal level was set to the 99% quantile. For better image contrasting, 100% color intensity of the color map was used. Averaged spectra for MALDI-TOF and MALDI-FTICR datasets were exported as an ASCII file and imported into the mMass software v 5.5[44]. Spectra acquired by MALDI-TOF were internally re-calibrated utilizing known compounds, reaching mass accuracy of 5 ppm.

Spectra acquired by MALDI-FTICR were processed without recalibration. A publicly available metabolite database was downloaded from www.hmdb.ca (v5), and only features annotated by the provider as “quantified” and “detected” were considered for putative annotations. MALDI-TOF spectra were annotated within ±10 ppm interval. MALDI-FTICR spectra of liver after ~35% hepatectomy were assigned within ±3.5 ppm error (Supplementary Table 2), and spectra from ~60% hepatectomy were assigned with ±2.5 ppm interval (Supplementary Table 3). Only $[M\text{-}H]^-$ ions were considered. To correctly annotate ^{15}N isotope variants, we implemented a new function into our in-house modification of the mMass software (https://github.com/marta-kaliaeva/mmass-extended) (Supplementary Table 4 and Supplementary Table 5). Molecules with a non-labeled nitrogen atom are further referred in text as m + 0 (no mass shift from the molecular weight of the non-labeled molecule), m + 1 (one ^{15}N atom, mass shift + 1 Da) and m + 2 (two ^{15}N atoms, mass shift + 2 Da).

For image analysis intensities, metabolites were displayed at a gray scale, and images (8-bit depth, resulting in signal levels from 0 to 255) were exported as PNG files into the FIJI software (ImageJ 1.54f). Intensities were reported as surface spanning from portal to central vein, respectively, with a depicted line of 10-pixel thickness. Intensity profile data were exported as .csv files and processed in the R software (www.r-project.org). For isotope enrichment ratios, intensity data for the given peak and sample were exported as.csv files and processed in the R software. Isotope ratio was reported as a fraction of all possible nitrogen isotope variations.

LC-MS and LC-MS data processing

A Q-Exactive orbitrap mass spectrometer with an Ion Max source and HESI II probe attached to the Vanquish Horizon UHLPC system was used to evaluate polar metabolites. The liquid chromatography – mass spectrometry (LC-MS) system underwent weekly cleaning and calibration with positive and negative Pierce ESI Ion Calibration Calmix (Thermo Scientific). To prepare samples for polar metabolite extraction, snap-frozen liver samples from 3 to 5 biological replicates after ~35% PHx were pulverized, and ~10 mg of tissue was vortexed in 60% cold methanol (− 20 °C) for 10 min. 500 µl of cold chloroform (− 20 °C) was added to the mixture and vortexed for 10 min. The solution was centrifuged at maximum speed for 10 min at 4 °C, and the top layer (polar fraction) was collected for polar metabolite analysis. 2 µl of the sample adjusted to 2 µg protein was run through a SeQuant ZIC-pHILIC 5 µm 150 × 2.1 mm analytical column (Sigma) with a 2.1 × 20 mm guard column (Sigma) attached to the front end. The column oven was set to 25 °C, and the autosampler was set to 4 °C. Buffer A comprised 20 mM ammonium carbonate (Sigma) and 0.1% ammonium hydroxide (Sigma) in HPLC-grade water (Sigma), and buffer B compromised 100% acetonitrile (Sigma). The liquid chromatography was set to the flow

rate of 0.15 ml/min. The metabolites were separated using the linear gradient from 80% buffer B to 20% buffer B over the course of 20 min, followed by an increasing gradient from 20% buffer B to 80% buffer B for 0.5 min, and by isocratic flow at 80% buffer B for 7.5 min. The mass spectrometer was set to full scan, polarity switching mode, with the spray voltage set to 4.0 kV, heated capillary to 350 °C, and the HESI probe to 30 °C. The MS data were acquired in the mass range of 70–1000 *m/z*. The sheath gas flow was set to 10 units, auxiliary gas to 1 unit, and sweep gas flow to 1 unit. Resolution of scans was set to 70,000, AGC target to 10^6, and maximum injection time to 20 ms. An additional scan between 220 and 700 *m/z* was used to enhance nucleotide detection in the negative mode, together with the maximum injection time set to 80 ms.

For LC-MS/MS measurements after ~60% hepatectomy, liver samples from 4 to 5 biological replicates were processed the same way as for MALDI-FTICR-MS/MS measurements, with the exception that the methanol/acetonitrile/water (4:4:2, v/v) solvent mixture was added at the ratio of 10 µl of solvent per mg of tissue. For measurement, Orbitrap IDX (Thermo Scientific) with an Optamax source and HESI probe, attached with Vanquish Horizon UHPLC, was used. 2 µl of the solution was injected into the iHILIC-(P) Classic 100 × 2.1 mm, 5 µm, 200 Å (HILICON) analytical column with iHILIC-(P) Classic 20 × 2.1 mm, 5 µm, 200 Å (HILICON) guard column. The column compartment was preheated to 40 °C. Mobile phase A contained 20 mM ammonium formate (Merck) with pH adjusted to 7 was used. Mobile phase B contained 95% acetonitrile with 10 mM ammonium formate. Flow rate was set to 200 µl/min. Chromatography was as follows: linear gradient from 95% to 42% buffer B for 14 min, followed by linear gradient from 42% to 95% of buffer B for 1 min, followed by isocratic flow of 90% buffer B for 1 min. The mass spectrometer was set to switch between full scan (100–1000 *m/z*) and ddMS2 in 0.6 s in negative polarity. Electrospray voltage was set to 2500 V, with Sheath Gas to 50 (Arb unit), Aux gas to 10, Sweep gas to 1. The ion transfer tube was set to 300 °C, vaporizer temperature to 350 °C. Orbitrap resolution was set to 60,000 for full scan. Peak intensities are reported as the area under the curve, and only $[M\text{-}H]^-$ ions were considered. Average peak mass for distinct metabolites was used to annotate peaks with the mMass software and the database from www.hmdb.ca (v5). Only features annotated by the provider as "quantified" and "detected" were considered for putative annotations within ± 1.5 ppm interval (Supplementary Table 6). For the ddMS2 Orbitrap, resolution was set to 15,000. Collision energies for the ddMS2 scan were set for 20, 30 and 40 in the stepped collision energy mode. Maximum injection time was set to 118 ms for full scan 80 ms for ddMS2. Aspartate, citrulline, glutamine, glutamate, orotate, uridine 5′-monophosphate, dihydroorotate, carbamoylaspartate, uridine, ornithine, and BAY-2402234 were fragmented. Spectra similarity score was assessed using the mzCloud standalone application (Supplementary Fig. 13 and Supplementary Table 7). Putative structure annotations were adapted from www.mzcloud.org, www.hmdb.ca, and https://cfmid.wishartlab.com/. Chemical structures were drawn in ChemSketch software v2023.1.2, (ACD/Labs).

Raw data were processed by MZmine v 4.5.20 software (mzio) with the retention time tolerance ± 20 s and mass tolerance ± 0.0015 *m/z*. For isotope enrichment ratios, areas under the curve for the given peak and sample were exported as.csv files and processed in the R software. Isotope ratio was reported as a fraction of all possible nitrogen isotope variations.

Immunofluorescence imaging

Tissue slices mounted on Superfrost slides were fixed with 4% paraformaldehyde (Sigma, P6148), washed twice with 0.1% Tween-20 (Sigma, P2287) in phosphate-buffered saline (0.1% PBT), and blocked with 0.5% bovine serum albumin (BSA, Sigma A3294) in 0.1% PBT (blocking buffer) for 1 h at room temperature. This was followed by overnight incubation with primary antibodies diluted in the blocking buffer. The sections were subsequently washed 3 times with 0.1% PBT and incubated with fluorescence-conjugated secondary antibodies (Invitrogen, A11029, A11012, A21245, A11006; diluted at 1:500 in 0.1% PBT) for 3 h. The sections were finally washed twice with 0.1% PBT for 5 min and mounted on coverslips using the Vectashield mounting medium with DAPI (Vector Laboratories, H-1200-10).

The following primary antibodies were used: E-cadherin (Cell Signaling, 14472; 1:100), glutamine synthetase (GS, Abcam, ab73593; 5 µg/ml), GS (Santa Cruz, sc-74430; 4 µg/ml), glutaminase-2 (GLS2, Abcam, 113509; 20 µg/ml), carbamoyl phosphate synthase-1 (CPS1, Abcam, ab3682; 1:500), CD31 (DIANOVA, DIA-310; 1:10). To detect proliferating cells labeled with EdU in the tissue sections using the click chemistry method, the sections were incubated for 1 h with a reaction cocktail consisting of 10 µM fluorescent azide (Thermo Fisher Scientific, A10277), 2 mM $CuSO_4$ (Sigma, 7758-98-7), and 20 mg/ml sodium ascorbate (Sigma, A4034) after the fixation, blocking, and washing steps, and prior to primary antibody application described above. Stained tissues were scanned using AxioScan.Z1 (Zeiss, Germany) fitted with a 10x objective, and processed with Zen 2 software (blue edition; Zeiss, Germany). Images were also acquired using the Leica TCS SP8 (Leica Biosystems, Germany) confocal microscope and processed using the Leica LAS-X (Leica Biosystems) software. All images acquired were exported as PNG or TIFF files.

Western blotting

Frozen liver samples (~ 50 µg) were homogenized and lysed in the radioimmunoprecipitation assay (RIPA) lysis buffer (20 mM Tris, pH 7.5; 150 mM NaCl; 1 mM EDTA; 1 mM EGTA; 1% NP-40; 0.1% SDS; 0.5% sodium deoxycholate) with a protease inhibitor (1:100) (cat. 3910202; Serva). Protein concentration was quantified using the BCA method (Pierce Biotechnology). Protein (15–25 µg) was separated by SDS-PAGE and then transferred onto a nitrocellulose membrane. The membrane was probed with the following antibodies: anti-MCM2 (NBP2-33953; Novus Biologicals), anti-PCNA (sc-25280; Santa Cruz), anti-P-HH3 (3642; Cell Signaling), anti-DHODH (14877-1-AP; Proteintech), anti-CAD (93925; Cell Signaling), anti-OTC (ab203859; Abcam), anti-UMPS (sc-398086; Santa Cruz), anti-CPS1 (ab3682; Abcam), anti-GOT1 (ab189863; Abcam), anti-GDH (12793S; Cell Signaling), and anti-β-actin (3700; Cell Signaling). Immunodetection was performed using the ECL Western Blotting Substrate (Thermo Fisher). Full blots are supplied in the Source Data file.

DHODH-dependent respiration

To evaluate DHODH-dependent respiration in liver tissue samples, snap frozen tissue samples were homogenized using a PBI-Shredder (Oroboros) in the Mir05 medium (0.5 mM EGTA, 3 mM $MgCl_2$, 60 mM K-lactobionate, 20 mM taurine, 10 mM KH_2PO_4, 110 mM sucrose, 1 g/l essential fatty acid-free bovine serum albumin, 20 mM Hepes, pH 7.1 at 30 °C). The homogenate was transferred to the chamber of the Oxygraph-2k instrument (Oroboros), and respiration evaluation conducted at 37 °C. DHODH-dependent respiration was corrected by subtracting the residual respiration rate remaining after addition of 30 µM teriflunomide from the respiration rate observed in the presence of 0.5 µM rotenone, 1 mM dihydroorotate, 3 mM ADP, and 10 µM cytochrome c. To validate the suitability of using snap-frozen tissue samples for the assay, freshly collected liver samples were assayed and compared with their corresponding snap-frozen liver samples under several conditions, as indicated in Supplementary Fig. 14.

DHODH activity assay

DHODH activity was assessed following a modified protocol[45]. Briefly, fresh-frozen tissue samples were homogenized using the PBI-Shredder (Oroboros) in water. The homogenates were then incubated in a solution containing 160 mM K_2CO_3-HCl (pH 8.0), 400 µM DHO, and 80 µM decylubiquinone at 37 °C for 60 min, while the reference sample

was maintained on ice. The reaction mixture was then supplemented with 20 mM K_2CO_3, 2 mM $K_3[Fe(CN)_6]$, and 1 mM 4-(trifluoromethoxy) benzamidoxime (4-TFMBAO), followed by heating at 80 °C for 4 min. The reaction was stopped by rapid cooling on ice, and fluorescence intensity was read using the Infinite M200 plate reader (Tecan), with the excitation and emission wavelengths set at 320 nm and 420 nm, respectively. To generate a calibration curve, lysate-free samples containing 0.5, 0.75, and 1 μM orotic acid were used.

Statistical analysis and reproducibility

Data are mean values ± standard deviation (S.D.) of at least three independent experiments. In mouse experiments, experimental groups of 3–15 randomly allocated animals were used, unless stated otherwise. No statistical method was used to predetermine sample size. Non-paired parametric data were compared with Student's *t* test using GraphPad Prism Software (7.0), where a *p*-value of < 0.05 was considered statistically significant. Images are representative of at least three independent experiments. The investigators were blinded to allocation during experiments and outcome assessment.

Reporting summary

Further information on research design is available in the Nature Portfolio Reporting Summary linked to this article.

Data availability

All data supporting the findings of this study are available within the paper and its Supplementary Information. Source Data are provided with this paper. The MALDI images used in this study are available in the Metaspace database under the following link: https://metaspace2020.org/project/kucera-2025. Source data are provided in this paper.

References

1. Du, Y. et al. Mouse models of liver parenchyma injuries and regeneration. *Front. Cell Dev. Biol.* **10**, 903740 (2022).
2. Michalopoulos, G. K. & DeFrances, M. C. Liver regeneration. *Science* **276**, 60–66 (1997).
3. Fausto, N., Campbell, J. S. & Riehle, K. J. Liver regeneration. *Hepatology* **43**, S45–S53 (2006).
4. Michalopoulos, G. K. & Bhushan, B. Liver regeneration: biological and pathological mechanisms and implications. *Nat. Rev. Gastro Hepat.* **18**, 40–55 (2021).
5. Tamori, Y. & Deng, W. M. Tissue repair through cell competition and compensatory cellular hypertrophy in postmitotic epithelia. *Dev. Cell* **25**, 350–363 (2013).
6. Diril, M. K. et al. Cyclin-dependent kinase 1 (Cdk1) is essential for cell division and suppression of DNA re-replication but not for liver regeneration. *Proc. Natl. Acad. Sci. USA* **109**, 3826–3831 (2012).
7. Locasale, J. W. & Cantley, L. C. Metabolic flux and the regulation of mammalian cell growth. *Cell Metab.* **14**, 443–451 (2011).
8. Caldez, M. J. et al. Metabolic remodeling during liver regeneration. *Dev. Cell* **47**, 425 (2018).
9. Tan, V. W. T. et al. SLAM-ITseq identifies that Nrf2 induces liver regeneration through the pentose phosphate pathway. *Dev. Cell* **59**, 898–910 (2024).
10. Huang, J. S. & Rudnick, D. A. Elucidating the metabolic regulation of liver regeneration. *Am. J. Pathol.* **184**, 309–321 (2014).
11. Huppert, S. S. & Schwartz, R. E. Multiple facets of cellular homeostasis and regeneration of the mammalian liver. *Annu Rev. Physiol.* **85**, 469–493 (2023).
12. Miettinen, T. P. & Björklund, M. Mitochondrial function and cell size: an allometric relationship. *Trends Cell Biol.* **27**, 393–402 (2017).
13. Mlettinen, T. P. et al. Identification of transcriptional and metabolic programs related to mammalian cell size. *Curr. Biol.* **24**, 598–608 (2014).
14. Tan, A. S. et al. Mitochondrial genome acquisition restores respiratory function and tumorigenic potential of cancer cells without mitochondrial DNA. *Cell Metab.* **21**, 81–94 (2015).
15. Dong, L. F. et al. Mitochondria on the move: Horizontal mitochondrial transfer in disease and health. *J. Cell Biol.* **222**, https://doi.org/10.1083/jcb.202211044 (2023).
16. Bajzikova, M. et al. Reactivation of dihydroorotate dehydrogenase-driven pyrimidine biosynthesis restores tumor growth of respiration-deficient cancer cells. *Cell Metab.* **29**, 399–416 (2019).
17. Martins, P. N., Theruvath, T. P. & Neuhaus, P. Rodent models of partial hepatectomies. *Liver Int* **28**, 3–11 (2008).
18. Christian, S. et al. The novel dihydroorotate dehydrogenase (DHODH) inhibitor BAY 2402234 triggers differentiation and is effective in the treatment of myeloid malignancies. *Leukemia* **33**, 2403–2415 (2019).
19. Sykes, D. B. et al. Inhibition of dihydroorotate dehydrogenase overcomes differentiation blockade in acute myeloid leukemia. *Cell* **167**, 171 (2016).
20. Salic, A. & Mitchison, T. J. A chemical method for fast and sensitive detection of DNA synthesis. *Proc. Natl Acad. Sci. USA* **105**, 2415–2420 (2008).
21. Santos, A. A. et al. Spatial metabolomics and its application in the liver. *Hepatology* **79**, 1158–1179 (2024).
22. Russell, J. O. & Camargo, F. D. Hippo signalling in the liver: role in development, regeneration and disease. *Nat. Rev. Gastro Hepat.* **19**, 297–312 (2022).
23. Zarrinpar, A. & Busuttil, R. W. Liver transplantation: past, present and future. *Nat. Rev. Gastroenterol. Hepatol.* **10**, 434–440 (2013).
24. Verma, A. K., Sharma, A., Subramaniyam, N. & Gandhi, C. R. Augmenter of liver regeneration: Mitochondrial function and steatohepatitis. *J. Hepatol.* **77**, 1410–1421 (2022).
25. Fausto, N., Brandt, J. T. & Kesner, L. Possible interactions between the urea cycle and synthesis of pyrimidines and polyamines in regenerating liver. *Cancer Res.* **35**, 397–404 (1975).
26. Mayer, D. et al. Expression of key enzymes of purine and pyrimidine metabolism in a hepatocyte-derived cell-line at different phases of the growth-cycle. *J. Cancer Res. Clin.* **116**, 251–258 (1990).
27. Usami, M. & Saitoh, Y. The effect of a nucleotide-nucleoside solution on hepatic regeneration in rats after partial hepatectomy and in primary monolayer culture of hepatocytes. *Nutrition* **13**, 365–368 (1997).
28. Boukalova, S. et al. Dihydroorotate dehydrogenase in oxidative phosphorylation and cancer. *Biochem.Biophys. Acta Mol. Basis Dis.* **1866**, 165759 (2020).
29. Brown, K. K., Spinelli, J. B., Asara, J. M. & Toker, A. Adaptive reprogramming of De novo pyrimidine synthesis is a metabolic vulnerability in triple-negative breast cancer. *Cancer Discov.* **7**, 391–399 (2017).
30. Yang, C. Z. et al. De novo pyrimidine biosynthetic complexes support cancer cell proliferation and ferroptosis defence. *Nat. Cell Biol.* **25**, 836 (2023).
31. Paluschinski, M. et al. Characterization of the scavenger cell proteome in mouse and rat liver. *Biol. Chem.* **402**, 1073–1085 (2021).
32. Brusilow, S. W. & Maestri, N. E. Urea cycle disorders: diagnosis, pathophysiology, and therapy. *Adv. Pediatr.* **43**, 127–170 (1996).
33. Bartl, M. et al. Optimality in the zonation of ammonia detoxification in rodent liver. *Arch. Toxicol.* **89**, 2069–2078 (2015).
34. Spinelli, J. B. et al. Metabolic recycling of ammonia *via* glutamate dehydrogenase supports breast cancer biomass. *Science* **358**, 941–946 (2017).
35. Lee, J. S. et al. Urea cycle dysregulation generates clinically relevant genomic and biochemical signatures. *Cell* **174**, 1559 (2018).

36. Rabinovich, S. et al. Diversion of aspartate in ASS1-deficient tumours fosters de novo pyrimidine synthesis. *Nature* **527**, 379 (2015).
37. Matsumoto, S. et al. Urea cycle disorders-update. *J. Hum. Genet* **64**, 833–847 (2019).
38. Grompe, M., Jones, S. N. & Caskey, C. T. Molecular-detection and correction of ornithine transcarbamylase deficiency. *Trends Genet.* **6**, 335–339 (1990).
39. Hosseini, M. et al. Energy metabolism rewiring precedes UVB-induced primary skin tumor formation. *Cell Rep.* **23**, 3621–3634 (2018).
40. Moriyama, M. et al. Decreased ureagenesis from alanine, but not from ammonia and glutamine, in the perfused rat liver after partial hepatectomy. *Hepatology* **23**, 1584–1590 (1996).
41. Kim, J. et al. CPS1 maintains pyrimidine pools and DNA synthesis in KRAS/LKB1-mutant lung cancer cells. *Nature* **546**, 168 (2017). +.
42. Helman, G., Pacheco-Colón, I. & Gropman, A. L. The urea cycle disorders. *Semin Neurol.* **34**, 341–349 (2014).
43. Kolářová, L. et al. Clusters of monoisotopic elements for calibration in (TOF) mass spectrometry. *J. Am. Soc. Mass Spectrom.* **28**, 419–427 (2017).
44. Strohalm, M., Kavan, D., Novák, P., Volný, M. & Havlícek, V. mMass 3: a cross-platform software environment for precise analysis of mass spectrometric data. *Anal. Chem.* **82**, 4648–4651 (2010).
45. Yin, S., Kabashima, T., Zhu, Q., Shibata, T. & Kai, M. Fluorescence assay of dihydroorotate dehydrogenase that may become a cancer biomarker. *Sci. Rep.* **7**, 40670 (2017).

Acknowledgements

This work was supported in part by grants 21-04607X and 23-04671S from the Czech Science Foundation and grant NU22-08-00160 from the Czech Health Foundation to J.N., grant 23-05303S from the Czech Science Foundation to S.B., grant NU23-03-00226 from the Czech Health Foundation to S.D., by grants from the Health Research Council of New Zealand and financial support from the Malaghan Institute to M.V.B., by a grant from the Charles University Grant Agency (GAUK 392222) to D.T.L., by funding from the Basic Science Research Program (Grant NRF2018R1A3B1052328) provided by the Ministry of Science, Information and Communication Technology and by Future Planning through the National Research Foundation to S.P., and by a grant 2020.04765.BD from FCT to G.L.O. The authors used the services of the Czech Centre for Phenogenomics at the Institute of Molecular Genetics, supported by the Czech Academy of Sciences RVO 68378050 and by the project LM2023036, Czech Centre for Phenogenomics, provided by the Ministry of Education, Youth and Sports of the Czech Republic. The authors acknowledge the Imaging Methods Core Facility at BIOCEV, an institution supported by the MEYS CR (LM2023050 Czech-BioImaging), for their support & assistance in this work and thank Matthew Vander Heiden for reading the manuscript and providing helpful suggestions.

Author contributions

Supervision: B.B.E. and J.N. Conceptualization: B.B.E. and J.N. Investigation, data curation and validation: B.B.E., L.K., J.B.S., A.B., D.L., K.K., G.L.O., P.B., D.T.L., K.B., S.B., R.Z., F.K., K.C., K.D., A.Y.B., S.D., E.B. and M.K. Writing (original draft): B.B.E. and J.N. Writing (review and editing): B.B.E., J.N., L.K. and M.V.B. Funding acquisition: J.N. Resources: R.S., J.P., V.H., L.V., S.P., P.M., Z.K. and P.J.O. All authors have read and approved the manuscript.

Competing interests

The authors declare no competing interests.

Additional information

Supplementary information The online version contains supplementary material available at https://doi.org/10.1038/s41467-025-65451-2.

Correspondence and requests for materials should be addressed to Berwini B. Endaya or Jiří Neužil.

Peer review information *Nature Communications* thanks Malcolm Alison, Benjamin Balluff and the other anonymous reviewer(s) for their contribution to the peer review of this work. A peer review file is available.